

Synthesis, Structure and Properties of Tetragonal $\text{Sr}_2M_3\text{As}_2\text{O}_2$ ($M_3 = \text{Mn}_3, \text{Mn}_2\text{Cu}$ and MnZn_2) Compounds Containing Alternating CuO_2 -Type and FeAs-Type Layers

R. Nath,^{1,*} V. O. Garlea,² A. I. Goldman,¹ and D. C. Johnston¹

¹*Ames Laboratory and Department of Physics and Astronomy, Iowa State University, Ames, Iowa 50011, USA*

²*Neutron Scattering Sciences Division, Oak Ridge National Laboratory, Oak Ridge, Tennessee 37831, USA*

(Dated: October 17, 2018)

Polycrystalline samples of $\text{Sr}_2\text{Mn}_2\text{CuAs}_2\text{O}_2$, $\text{Sr}_2\text{Mn}_3\text{As}_2\text{O}_2$, and $\text{Sr}_2\text{Zn}_2\text{MnAs}_2\text{O}_2$ were synthesized. Their temperature- and applied magnetic field-dependent structural, transport, thermal, and magnetic properties were characterized by means of x-ray and neutron diffraction, electrical resistivity ρ , heat capacity, magnetization and magnetic susceptibility measurements. These compounds have a body-centered-tetragonal crystal structure (space group $I4/mmm$) that consists of MO_2 ($M = \text{Zn}$ and/or Mn) oxide layers similar to the CuO_2 layers in high superconducting transition temperature T_c cuprate superconductors, and intermetallic $M\text{As}$ ($M = \text{Cu}$ and/or Mn) layers similar to the FeAs layers in high- T_c pnictides. These two types of layers alternate along the crystallographic c -axis and are separated by Sr atoms. The site occupancies of Mn, Cu and Zn were studied using Rietveld refinements of x-ray and neutron powder diffraction data. The temperature dependences of ρ suggest metallic character for $\text{Sr}_2\text{Mn}_2\text{CuAs}_2\text{O}_2$ and semiconducting character for $\text{Sr}_2\text{Mn}_3\text{As}_2\text{O}_2$ and $\text{Sr}_2\text{Zn}_2\text{MnAs}_2\text{O}_2$. $\text{Sr}_2\text{Mn}_2\text{CuAs}_2\text{O}_2$ is inferred to be a ferrimagnet with a Curie temperature $T_C = 95(1)$ K. Remarkably, we find that the magnetic ground state structure changes from a G-type antiferromagnetic structure in $\text{Sr}_2\text{Mn}_3\text{As}_2\text{O}_2$ to an A-type ferrimagnetic structure in $\text{Sr}_2\text{Mn}_2\text{CuAs}_2\text{O}_2$ in which the Mn ions in each layer are ferromagnetically aligned, but are antiferromagnetically aligned between layers.

PACS numbers: 74.70.-b, 75.40.Cx, 75.47.Lx, 65.40.Ba

I. INTRODUCTION

Superconductivity research was reinvigorated by the discovery of high temperature superconductivity in layered cuprates in 1986.¹ The highest superconducting transition temperature T_c of 164 K reported up to now for any material was achieved in $\text{HgBa}_2\text{Ca}_2\text{Cu}_3\text{O}_{8+\delta}$ under pressure.^{2,3} Recently a series of layered pnictide compounds $R\text{FeAsO}_{1-x}\text{F}_x$ ($R = \text{La}, \text{Ce}, \text{Pr}, \text{Nd}, \text{Sm},$ and Gd)⁴⁻⁸ and $\text{A}_{1-x}\text{K}_x\text{Fe}_2\text{As}_2$ ($A = \text{Ba}, \text{Sr}, \text{Ca},$ and Eu) (Refs. 9-13) and other pnictide families were discovered where T_c ranges up to 56 K. Both the cuprate and iron pnictide families of high- T_c compounds contain square lattice layers, of Cu and Fe, respectively. A principal difference between the cuprate and pnictide superconductors is in the detailed nature of the transition metal layers. In the cuprates, the oxygen atoms in the CuO_2 layers are situated directly between nearest-neighbor Cu atoms, the bonding in the plane is primarily Cu-O bonding, and the states at the Fermi energy E_F contain a large O $2p$ component. The high T_c in the cuprates is believed to be intimately related to the crystal geometry.¹⁴⁻¹⁶ In the FeAs-type compounds, on the other hand, the As atoms are arranged in layers on either side of the Fe square lattice layers, resulting in tetrahedral coordination of the Fe atoms by As. Strong direct Fe-Fe interactions cause the electron states at E_F to be dominated by states derived from the Fe d -orbitals.

A real challenge is to search for new materials with even higher T_c values. As is evident from the previous studies, T_c is intimately related to the arrangement, sep-

aration, and atomic constituents of the transition metal layers. Therefore it may be possible to achieve an enhanced T_c by tuning certain structural and/or chemical parameters. Recently Volkova¹⁷ and Ozawa *et al.*¹⁸ reported comparative studies of the structural properties of different layered compounds and suggested that $\text{A}_2\text{Mn}_3\text{Pn}_2\text{O}_2$ ($A = \text{Ba}, \text{Sr}$; pnictogen $\text{Pn} = \text{As}, \text{Sb}$) type compounds might serve as parent compounds for high- T_c superconductivity. The structure of this class of compounds contains two different types of layers — an MO_2 layer similar to the CuO_2 layers in the high- T_c cuprates and an $M'\text{As}$ layer similar to the FeAs layers in the pnictide superconductors.^{19,20} Magnetic and structural properties of some of these compounds have been studied via magnetization^{21,22} and neutron diffraction²⁰ measurements. There has also been much recent experimental interest in mixed layered chalcogenide oxide²³ and oxysulfide²⁴ compounds as potential candidates for high- T_c compounds and/or for other interesting magnetic and electronic properties.²⁵

The $\text{A}_2\text{Mn}_3\text{Pn}_2\text{O}_2$ compounds crystallize in the body-centered-tetragonal tetragonal space group $I4/mmm$. As shown in Fig. 1, the parent compound $\text{Sr}_2\text{Mn}_3\text{As}_2\text{O}_2$ has two inequivalent Mn sites. The Mn1 atoms are fourfold coordinated by O in a plane to form a CuO_2 -type square lattice as in the high- T_c cuprates. The Mn2 atoms are fourfold coordinated by As to form FeAs-type layers similar to the FeAs layers in the high- T_c pnictide superconductors. The CuO_2 -type and FeAs-type layers alternate along the crystallographic c axis and are separated by Sr layers. Each type of Mn atom has four nearest-

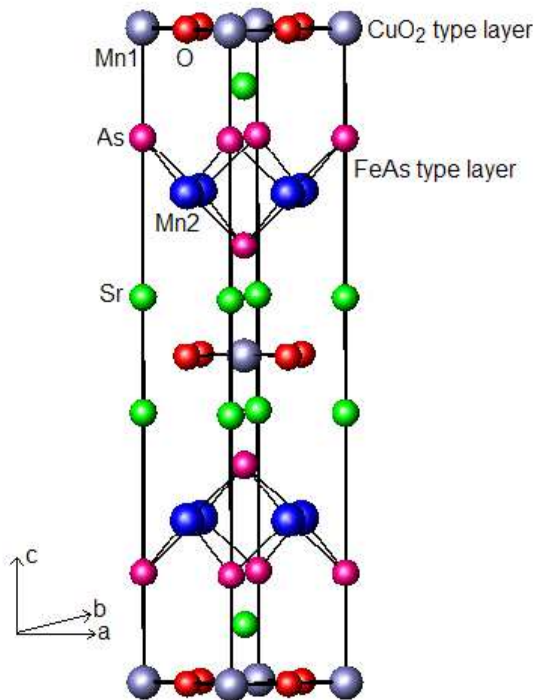


FIG. 1: (Color online) Crystal structure of $\text{Sr}_2\text{Mn}_3\text{As}_2\text{O}_2$ showing alternating CuO_2 -type and FeAs -type layers along the c -axis. These layers are separated by layers of Sr atoms.

neighbor Mn atoms within each plane, and four nearest-neighbors in each of the two adjacent planes. An interesting and potentially important aspect of this arrangement of the Mn atoms in adjacent layers is that the interactions between Mn1 and Mn2 are geometrically frustrated for antiferromagnetic ordering. Previous neutron diffraction measurements showed that there are no structural transitions down to 4 K that could serve to relieve the frustration.^{20,26}

The syntheses and magnetic measurements of $\text{Sr}_2\text{Zn}_2\text{MnAs}_2\text{O}_2$ and $\text{Sr}_2\text{Mn}_3\text{As}_2\text{O}_2$ have been previously reported.^{20,21,26,27} For $\text{Sr}_2\text{Mn}_3\text{As}_2\text{O}_2$, magnetic neutron diffraction measurements indicate the presence of two distinct types of magnetic sublattice.²⁰ The Mn2 sublattice undergoes long-range antiferromagnetic (AF) ordering at a Néel temperature $T_N = 340$ K in a G-type AF structure with an ordered moment of $3.4 \mu_B/\text{Mn}$ at 4 K, where μ_B is the Bohr magneton.²⁰ On the other hand, the Mn1 sublattice does not undergo long-range ordering down to 4 K but instead shows very weak magnetic reflections below 75 K where the most prominent reflection has a Warren line shape, which is indicative of two-dimensional short-range order.²⁰ Zero-field-cooled (ZFC) and field-cooled (FC) $\chi(T)$ data show a broad but weak maximum at 65 K and a bifurcation at 51 K.²¹ For $\text{Sr}_2\text{MnZn}_2\text{As}_2\text{O}_2$, ZFC and FC susceptibility data show a weak maximum at 65 K and a splitting around 30 K.²⁶ A Curie-Weiss fit to $\chi(T)$ at high T yields a positive Weiss temperature $\theta = 43$ K suggesting that the dominant interaction is ferromagnetic. However,

neutron diffraction experiments show no evidence for either short-range or long-range order down to 4 K.²⁶

Herein, we report the synthesis and detailed characterization of the $\text{Sr}_2\text{Mn}_3\text{As}_2\text{O}_2$ -type compound $\text{Sr}_2\text{Mn}_2\text{CuAs}_2\text{O}_2$. This compound has not been synthesized or studied before to our knowledge, although Cu-containing materials were previously suggested.²⁸ The goal was to synthesize a parent compound with CuO_2 layers as in the high- T_c layered cuprates, alternating with MnAs layers as in the FeAs-type materials, which upon doping might become a high- T_c superconductor. However, we found that although the compound with the desired composition does form, the Cu atoms do not go into the CuO_2 -type layers, but rather statistically occupy approximately half of the transition metal sites in the FeAs-type layers. We have characterized this material in detail as a function of temperature T and/or applied magnetic field H by means of x-ray and neutron diffraction, electrical resistivity ρ , heat capacity C_p , magnetization M and magnetic susceptibility χ measurements. For comparison, we also carried out detailed structure and property measurements on the above previously reported $\text{Sr}_2\text{Zn}_2\text{MnAs}_2\text{O}_2$ and $\text{Sr}_2\text{Mn}_3\text{As}_2\text{O}_2$ compounds.

The remainder of the paper is organized as follows. The synthesis and measurement details are given in Sec. II. The results of our x-ray and neutron structure analyses, magnetization and magnetic susceptibility, and heat capacity measurements are given in Sec. III. A discussion of our results is given in Sec. IV. A summary of our results and conclusions is given in Sec. V.

II. EXPERIMENTAL DETAILS

A. Sample Preparation

Polycrystalline samples of $\text{Sr}_2\text{Mn}_2\text{CuAs}_2\text{O}_2$, $\text{Sr}_2\text{Zn}_2\text{MnAs}_2\text{O}_2$, and $\text{Sr}_2\text{Mn}_3\text{As}_2\text{O}_2$ were prepared by solid state reaction techniques using SrO (99.9% pure), Mn (99.99% pure, Alfa-Aesar), Cu (99.99% pure, Fisher), Zn (99.99% pure, Alfa-Aesar), and As (99.9% pure, Alfa-Aesar) as starting materials. The SrO was prepared by heating SrCO_3 (99.99% pure, Aldrich) at 1300 °C in air for 12 h and cooling under vacuum. The stoichiometric mixtures of the starting materials were placed in an Al_2O_3 crucible that was then sealed inside an evacuated quartz tube. The samples were first heated to 610 °C at a rate of 80 °C/h, held there for 10 h and then heated to 980 °C and held there for 20 h. The samples were then progressively fired at 980 °C and 1000 °C for 30 h, each followed by one intermediate grinding and pelletization. All the sample handling was carried out inside a He-filled glove box.

B. X-ray, Magnetic Susceptibility, Heat Capacity, and Electrical Resistivity Characterization

The samples were characterized using a Rigaku Geigerflex powder diffractometer with a Cu target ($\lambda_{\text{ave}} = 1.54182 \text{ \AA}$). The magnetization $M(H, T)$ and magnetic susceptibility $\chi(T) \equiv M(H, T)/H$ were measured in the temperature T range $1.8 \text{ K} \leq T \leq 350 \text{ K}$ in applied fields up to 5.5 T. Zero-field-cooled (ZFC) and field-cooled (FC) magnetic susceptibilities were also measured as a function of T at $H = 100 \text{ Oe}$. The magnetic measurements were carried out using a commercial (Quantum Design) SQUID (superconducting quantum interference device) magnetometer. The DC resistivity $\rho(T)$ was measured with a standard four-probe technique using a current of 5 mA, and heat capacity $C_p(T)$ was measured on samples of mass $\sim 5 \text{ mg}$. The $\rho(T)$ and $C_p(T)$ measurements were performed on pieces of sintered pellets using a Quantum Design Physical Property Measurement System (PPMS).

C. Neutron Diffraction Measurements

Neutron powder diffraction measurements on both $\text{Sr}_2\text{Mn}_3\text{As}_2\text{O}_{10}$ and $\text{Sr}_2\text{Mn}_2\text{CuAs}_2\text{O}_{10}$ were carried out at the HB2A neutron powder diffractometer at the High Flux Isotope Reactor at Oak Ridge National Laboratory, using a wavelength of $\lambda = 1.536 \text{ \AA}$ provided by a vertically focusing Ge(115) monochromator. For data collection, the detector array consisting of 44 ^3He tubes was scanned in two segments to cover the total 2θ range of 4° to 150° , in steps of 0.05° . Overlapping detectors for a given step served to average the counting efficiency of each detector. More details about the HB2A instrument and data collection strategies can be found in Ref. 29. Measurements were made on approximately 5 g of sample held in a cylindrical vanadium container in a top-loading closed cycle refrigerator (4–300 K).

For the $\text{Sr}_2\text{Mn}_3\text{As}_2\text{O}_{10}$ sample, powder patterns were collected at $T = 375 \text{ K}$ (above T_N as reported by Brock et al.²⁰), 300 K, 150 K, 75 K and at 4 K, below the temperature where new magnetic reflections have been reported.²⁰ For $\text{Sr}_2\text{Mn}_2\text{CuAs}_2\text{O}_{10}$, powder patterns were collected at $T = 375 \text{ K}$, 300 K, 150 K, 60 K and at 4 K. Rietveld refinements were performed using the FULLPROF program.³⁰ Although both samples were relatively phase pure, small amounts of impurity phases of MnO ($\approx 2\text{--}3\%$) and a second, unidentified, phase were present. MnO orders antiferromagnetically below the Néel temperature $T_N \approx 118 \text{ K}$,³¹ and the associated magnetic peaks were identified during the refinements.

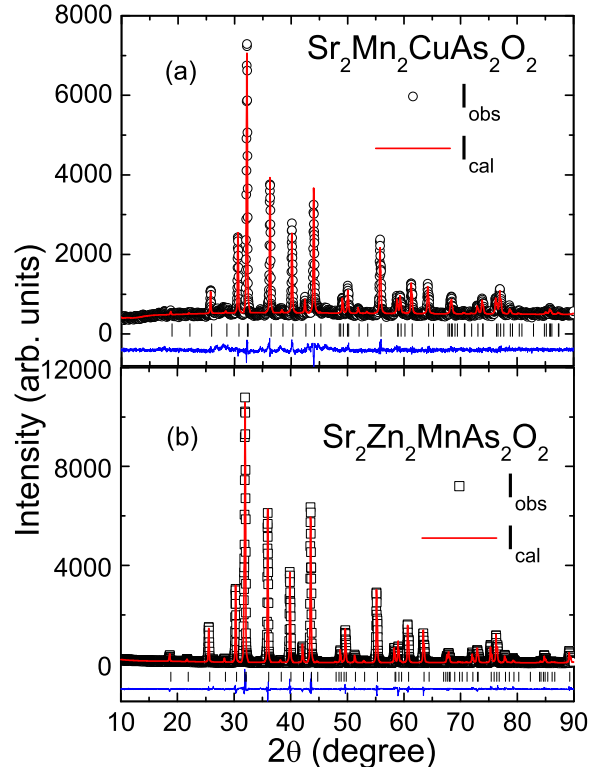


FIG. 2: (Color online) X-ray powder diffraction patterns (open circles) at room temperature for (a) $\text{Sr}_2\text{Mn}_2\text{CuAs}_2\text{O}_{10}$ and (b) $\text{Sr}_2\text{Zn}_2\text{MnAs}_2\text{O}_{10}$. The solid lines are Rietveld refinement fits with $I4/mmm$ space group. For $\text{Sr}_2\text{Mn}_2\text{CuAs}_2\text{O}_{10}$ the fit shown is for model (ii) discussed in the text.

TABLE I: Site occupancy models and quality of fit parameters R for $\text{Sr}_2\text{Mn}_2\text{CuAs}_2\text{O}_{10}$ from Rietveld refinements of powder XRD data at room temperature. The $2(a)$ site is the transition metal site in the CuO_2 -type layer, whereas the $4(d)$ site is the transition metal site in the FeAs -type layer.

Model	$2(a)$ site	$4(d)$ site	R (%)
(i)	Cu	Mn	16
(ii)	Mn	Mn and Cu	18
(iii)	Mn and Cu	Mn and Cu	13.7

III. RESULTS

A. Structure

The powder x-ray diffraction patterns indicated almost single phase samples of $\text{Sr}_2\text{Mn}_2\text{CuAs}_2\text{O}_{10}$ and $\text{Sr}_2\text{Zn}_2\text{MnAs}_2\text{O}_{10}$ while in $\text{Sr}_2\text{Mn}_3\text{As}_2\text{O}_{10}$, about 2.5% MnO impurity phase was detected. Rietveld refinements of the data were carried out using the GSAS package.³² The initial crystallographic parameters were taken from

TABLE II: Structure parameters for $\text{Sr}_2\text{Mn}_2\text{CuAs}_2\text{O}_2$ (space group $I4/mmm$, $Z = 2$ f.u./unit cell) refined from powder XRD data at room temperature for model (ii).

Atom	Wyckoff site	x	y	z	B (\AA^2)
Sr	4(<i>e</i>)	0	0	0.4104(1)	0.009(1)
Mn1	2(<i>a</i>)	0	0	0	0.023(3)
Cu	4(<i>d</i>)	0	0.5	0.25	0.041(4)
Mn2	4(<i>d</i>)	0	0.5	0.25	0.000
As	4(<i>e</i>)	0	0	0.1675(2)	0.018(2)
O	4(<i>c</i>)	0	0.5	0	0.053(9)

the previous reports on $\text{Sr}_2\text{Mn}_3\text{As}_2\text{O}_2$ (Refs. 19 and 20) and $\text{Sr}_2\text{Zn}_2\text{MnAs}_2\text{O}_2$ (Ref. 26). In addition to the other parameters, the transition metal site [2(*a*) (0 0 0) and 4(*d*) (0 0.5 0.25)] occupancies were also refined. We considered three models for $\text{Sr}_2\text{Mn}_2\text{CuAs}_2\text{O}_2$ as listed in Table I. In model (ii), the 4(*d*) site is occupied by 50% Mn and 50% Cu and in model (iii), the 2(*a*) site is occupied by 50% Mn and 50% Cu and the 4(*d*) site by 75% Mn and 25% Cu. The relatively large R value in each case is mainly due to our inability to fit the background precisely. Since the R values in the three cases are nearly the same, we cannot draw any conclusions about the respective occupancies of the 2(*a*) and 4(*d*) sites. Figure 2(a) shows the Rietveld refinement fit to the powder x-ray diffraction pattern obtained using model (ii).

On the other hand, for $\text{Sr}_2\text{Zn}_2\text{MnAs}_2\text{O}_2$, using refinements similar to those above, Mn and Zn were found to only occupy the CuO_2 -type and FeAs -type layers, respectively. Figure 2(b) presents the Rietveld refinement for $\text{Sr}_2\text{Zn}_2\text{MnAs}_2\text{O}_2$, for which the R -factor is $R_{\text{wp}} = 6\%$. This result is very similar to the previous report on $\text{Sr}_2\text{Zn}_2\text{MnAs}_2\text{O}_2$ where powder neutron diffraction data indicated complete site occupancy of the oxide layer by Mn and occupancy of the pnictide layer by 94% Zn and 6% Mn.²⁶ It was also mentioned that the lack of full occupancy in the pnictide layer by Zn might be due to the loss of Zn during synthesis since a significant amount of Zn_2As_3 separated from the starting materials by gas phase diffusion. Moreover similar site occupancies were found for the Ba analogue $\text{Ba}_2\text{Zn}_2\text{MnAs}_2\text{O}_2$.²⁷

The lattice parameters obtained at room temperature are [$a = 4.0833(2)$ \AA , $c = 18.5919(9)$ \AA], [$a = 4.12757(6)$ \AA , $c = 18.6941(4)$ \AA], and [$a = 4.14160(7)$ \AA , $c = 18.8177(4)$ \AA] for $\text{Sr}_2\text{Mn}_2\text{CuAs}_2\text{O}_2$, $\text{Sr}_2\text{Zn}_2\text{MnAs}_2\text{O}_2$, and $\text{Sr}_2\text{Mn}_3\text{As}_2\text{O}_2$, respectively. The values for $\text{Sr}_2\text{Zn}_2\text{MnAs}_2\text{O}_2$ and $\text{Sr}_2\text{Mn}_3\text{As}_2\text{O}_2$ are close to the previously reported ones²⁶ while for the new compound $\text{Sr}_2\text{Mn}_2\text{CuAs}_2\text{O}_2$, the values are slightly smaller than those reported for the other two compounds. Some parameters obtained from the Rietveld refinements on $\text{Sr}_2\text{Mn}_2\text{CuAs}_2\text{O}_2$ are listed in Table II.

Our main goal was to achieve a material with Fe occupying the MnAs layer and Cu occupying the MnO_2 layer.

TABLE III: Compositions synthesized during unsuccessful attempts to obtain single-phase compounds with the $\text{Sr}_2\text{Mn}_3\text{As}_2\text{O}_2$ -type structure.

$\text{Sr}_2\text{Fe}_3\text{As}_2\text{O}_2$	$\text{Sr}_2\text{Zn}_2\text{CuAs}_2\text{O}_2$
$\text{Sr}_2\text{Fe}_3\text{P}_2\text{O}_2$	$\text{Sr}_2\text{Mn}_2\text{CuSb}_2\text{O}_2$
$\text{Sr}_2\text{Fe}_3\text{Sb}_2\text{O}_2$	$\text{Ca}_2\text{Mn}_2\text{CuAs}_2\text{O}_2$
$\text{Sr}_2\text{Fe}_2\text{CuAs}_2\text{O}_2$	$\text{Sr}_2\text{MnCu}_2\text{As}_2\text{O}_2$
$\text{Sr}_2\text{Fe}_2\text{CuSb}_2\text{O}_2$	$\text{Sr}_2\text{Zn}_2\text{FeAs}_2\text{O}_2$
$\text{Ca}_2\text{Fe}_2\text{CuAs}_2\text{O}_2$	$\text{Sr}_2\text{Mn}_2\text{FeAs}_2\text{O}_2$
$\text{Sr}_2\text{Mn}_2\text{CuP}_2\text{O}_2$	$\text{Sr}_2\text{Ni}_2\text{ZnAs}_2\text{O}_2$

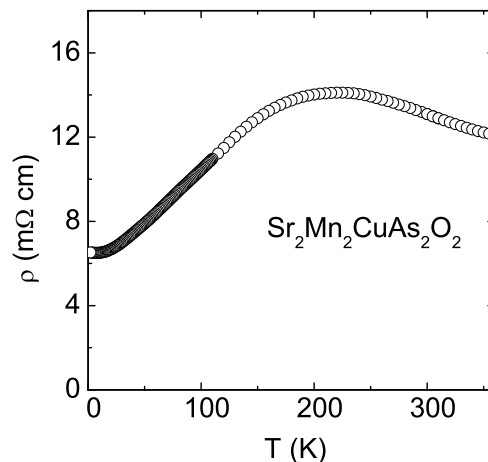


FIG. 3: DC electrical resistivity ρ versus temperature T of $\text{Sr}_2\text{Mn}_2\text{CuAs}_2\text{O}_2$.

With this objective in mind, in addition to the three compounds discussed in this paper that were obtained in nearly single-phase form, we attempted to synthesize fourteen other compounds with the $\text{Sr}_2\text{Mn}_3\text{As}_2\text{O}_2$ -type structure that are listed in Table III. We did not obtain single-phase materials with these compositions and these are therefore not discussed further.

B. Electrical Resistivity Measurements

Figure 3 shows $\rho(T)$ for $\text{Sr}_2\text{Mn}_2\text{CuAs}_2\text{O}_2$, and Fig. 4(a) shows $\rho(T)$ for $\text{Sr}_2\text{Mn}_3\text{As}_2\text{O}_2$ and $\text{Sr}_2\text{Zn}_2\text{MnAs}_2\text{O}_2$. With decreasing T , $\rho(T)$ for $\text{Sr}_2\text{Mn}_2\text{CuAs}_2\text{O}_2$ first increases, then shows a broad maximum at about 200 K, and then decreases to a residual resistivity of about 6.5 $\text{m}\Omega \text{ cm}$ at 2 K. The decrease in $\rho(T)$ towards a constant value for $T \rightarrow 0$ K suggests a metallic ground state. The negative coefficient of resistivity at high T and an overall magnitude of resistivity higher than expected for a metal may be associated with trace amounts of high-resistivity

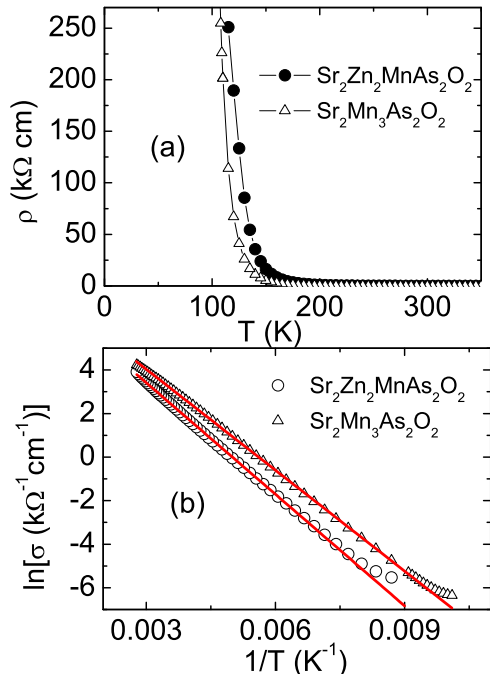


FIG. 4: (Color online) (a) DC electrical resistivity ρ of $\text{Sr}_2\text{Mn}_3\text{As}_2\text{O}_2$ and $\text{Sr}_2\text{Zn}_2\text{MnAs}_2\text{O}_2$ versus temperature T . (b) $\ln(\sigma)$ versus $1/T$. The red straight lines are linear fits to the data between 150 and 300 K.

impurities in the grain boundaries of the polycrystalline sample as often occurs in oxides.

In contrast, for $\text{Sr}_2\text{Mn}_3\text{As}_2\text{O}_2$ and $\text{Sr}_2\text{Zn}_2\text{MnAs}_2\text{O}_2$, ρ increases monotonically with decreasing T towards large values, pointing towards an insulating ground state of the compounds. Data below 115 K were not obtained for these compounds since the resistances of the samples below this temperature exceeded the measurement limit of the equipment. Figure 4(b) shows a plot of $\ln\sigma$ versus $1/T$ where $\sigma = 1/\rho$ is the conductivity. We fitted the data between 120 K and 300 K and between 150 and 300 K by the expression $\ln\sigma = A + \Delta/(k_B T)$ as shown in Fig. 4(b) where A is a constant and Δ is the activation energy, yielding $\Delta = 133(4)$ meV and $147(5)$ meV for $\text{Sr}_2\text{Mn}_3\text{As}_2\text{O}_2$ and $\text{Sr}_2\text{Zn}_2\text{MnAs}_2\text{O}_2$, respectively. We infer that $\text{Sr}_2\text{Mn}_3\text{As}_2\text{O}_2$ and $\text{Sr}_2\text{Zn}_2\text{MnAs}_2\text{O}_2$ are narrow band gap semiconductors.

C. Magnetization and Magnetic Susceptibility Measurements

1. $\text{Sr}_2\text{Zn}_2\text{MnAs}_2\text{O}_2$

The magnetic susceptibility $\chi \equiv M/H$ as a function of temperature T is shown in Fig. 5(a) for $\text{Sr}_2\text{Zn}_2\text{MnAs}_2\text{O}_2$ measured at an applied magnetic field $H = 1$ T. χ in-

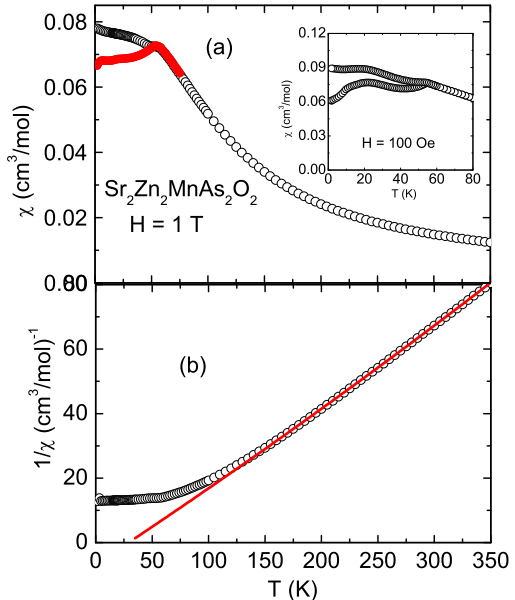


FIG. 5: (Color online) (a) ZFC (red, lower data set) and FC (black, upper data set) magnetic susceptibility χ of $\text{Sr}_2\text{Zn}_2\text{MnAs}_2\text{O}_2$ versus temperature T in magnetic field $H = 1$ T. Inset: ZFC and FC susceptibilities versus T at $H = 100$ Oe. (b) Inverse magnetic susceptibility χ^{-1} versus T . The solid line is a Curie-Weiss fit to the high temperature data between 175 and 350 K.

creases with decreasing T , suggesting local moment magnetism. The ZFC and FC susceptibilities show a bifurcation below ≈ 50 K, as also seen for $H = 100$ Oe in the inset of Fig. 5(a), indicating the occurrence of magnetic ordering of some type below that temperature.

To fit the molar magnetic susceptibility data of a local moment system in the paramagnetic state, one often uses the expression

$$\chi = \chi_0 + \frac{C}{T - \theta}, \quad (1)$$

where χ_0 is the temperature-independent contribution. The second term is the Curie-Weiss law with Curie constant $C = N_A \mu_{\text{eff}}^2 / (3k_B)$ and Weiss temperature θ , where N_A is Avogadro's number, μ_{eff} is the effective magnetic moment per formula unit, and k_B is Boltzmann's constant. For an insulator, one has

$$\chi_0 = \chi_{\text{core}} + \chi_{\text{VV}} \quad (2)$$

where χ_{core} is the core diamagnetism and χ_{VV} is the Van Vleck paramagnetism. χ_{core} can be calculated assuming an ionic model for individual atoms in the oxidation states Sr^{2+} , Mn^{2+} , Cu^{2+} , Zn^{2+} , As^{3-} , and O^{2-} ,³³ yielding $\chi_{\text{core}} = -1.6 \times 10^{-4}$ cm³/mol. The value of χ_{VV} is not easily accessible for a given compound, but when calculated it is often found to have about the same magnitude as χ_{core} , but with a positive instead of negative

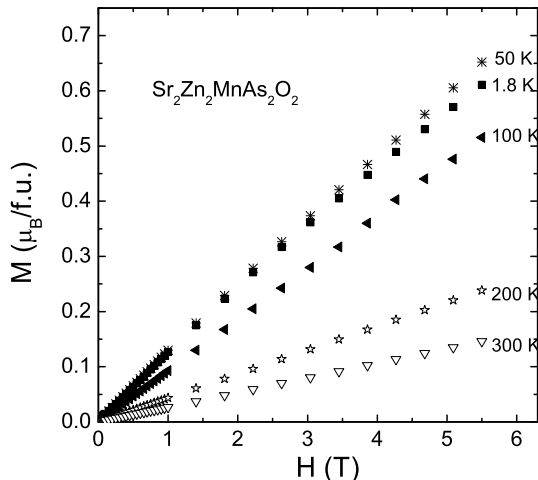


FIG. 6: Magnetization M versus applied magnetic field H isotherms for $\text{Sr}_2\text{Zn}_2\text{MnAs}_2\text{O}_2$ at the indicated temperatures.

sign, yielding a net small and often negligible value of χ_0 in local moment systems.

Fitting $\chi(T)$ by Eq. (1) in the high- T region 175–350 K yielded value of $\chi_0 = -6.8(5) \times 10^{-4} \text{ cm}^3/\text{mol}$ that is far more negative than the above χ_{core} value and hence is unphysical. Therefore, we fitted the data by fixing χ_0 to either χ_{core} or zero in Eq. (1), over different temperature ranges from 175 K to 350 K. Setting $\chi_0 = \chi_{\text{core}} = -1.6 \times 10^{-4} \text{ cm}^3/\text{mol}$ yielded $C = 3.92(2) \text{ cm}^3 \text{ K}/\text{mol}$ and $\theta = 39(1) \text{ K}$, whereas setting $\chi_0 = 0$ yielded $C = 3.84(3) \text{ cm}^3 \text{ K}/\text{mol}$ and $\theta = 41.6(16) \text{ K}$. Taking into account both values of C yields an effective moment $\mu_{\text{eff}} = 5.57(5) \mu_{\text{B}}/\text{f.u.}$ These parameters are in agreement with the previously reported values.²⁶ The positive value of θ indicates that the dominant interactions in the compound are ferromagnetic. The formal oxidation state of the Mn ions is +2, corresponding to a d^5 electronic configuration. The observed μ_{eff} is somewhat smaller than the value $g\sqrt{S(S+1)}\mu_{\text{B}} = 5.92 \mu_{\text{B}}$ expected for high-spin ($S = 5/2$) Mn^{+2} with g -factor $g = 2$, possibly due to hybridization effects as apparently occurs in BaMn_2As_2 .³⁴ For $S = 2$ with $g = 2$, one would instead obtain $\mu_{\text{eff}} = 4.90 \mu_{\text{B}}$, significantly smaller than the observed value.

Figure 6 shows $M(H)$ isotherms at different temperatures between 1.8 K to 300 K for H up to 5.5 T. One sees that M is nearly proportional to H at all temperatures down to 1.8 K. This observation, and the bifurcation between the FC and ZFC susceptibility data below ≈ 50 K in the inset of Fig. 5(a), are consistent with the conclusion in Ref. 26 that spin-glass ordering occurs below ~ 50 K.

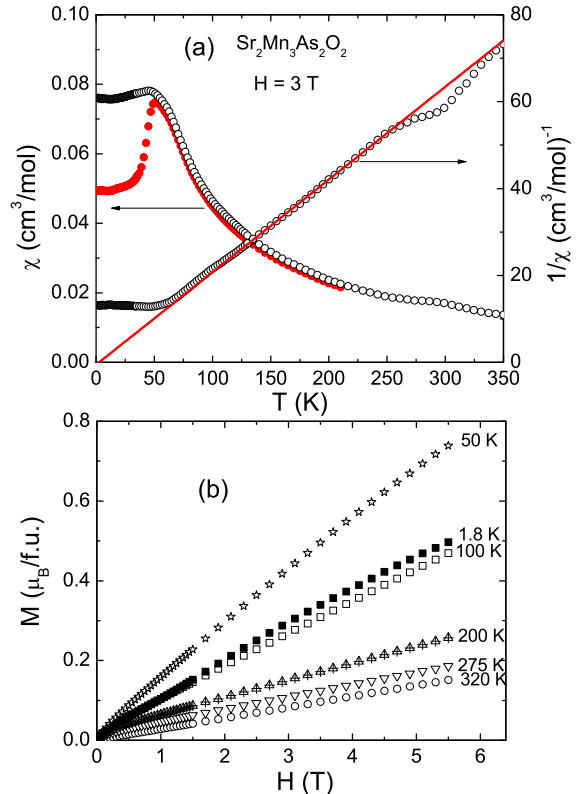


FIG. 7: (Color online) (a) Zero-field-cooled ZFC (lower red data set) and field-cooled FC (upper black data set) magnetic susceptibility χ (left-hand axis) and χ^{-1} (right-hand axis) of $\text{Sr}_2\text{Mn}_3\text{As}_2\text{O}_2$ versus temperature T in magnetic field $H = 3 \text{ T}$. The data are (approximately) corrected for the contribution of $\approx 0.79 \text{ mol}\%$ of ferromagnetic MnAs impurity phase (see text). The solid line is a Curie-Weiss fit of the data from 130 K to 250 K. (b) Magnetization M versus applied magnetic field H isotherms measured at the indicated temperatures.

2. $\text{Sr}_2\text{Mn}_3\text{As}_2\text{O}_2$

Figure 7(a) shows the ZFC and FC $\chi(T)$ of $\text{Sr}_2\text{Mn}_3\text{As}_2\text{O}_2$ measured at 3 T. A small step in $\chi(T)$ was observed at $T \simeq 310 \text{ K}$, even after correcting (see below) for a small amount of MnAs impurity which is known to have a first order ferromagnetic transition at 318 K.³⁵ The ZFC and FC $\chi(T)$ data show a significant splitting at 50 K suggesting a possible spin-glass transition, a two-dimensional magnetic ordering transition,²⁰ or in view of our magnetic neutron diffraction data below, possibly a three-dimensional magnetic transition.

$M(H)$ isotherms were measured at different temperatures to test for the presence of MnAs ferromagnetic impurity phase in the sample and are shown in Fig. 7(b). At 320 K, M is proportional to H over the whole field range. Below $\sim 300 \text{ K}$, nonlinearity was observed in the $M(H)$

curves below 0.5 T suggesting a small ferromagnetic MnAs impurity contribution to the magnetization which saturates by about 1 T. We did not, however, observe any peaks in our x-ray diffraction measurements corresponding to the fingerprint of MnAs, indicating that the MnAs impurity concentration is less than 2% of the sample. In order to quantitatively estimate the MnAs impurity concentration, we fitted the $M(H)$ isotherms for $H = 2.5$ to 5.5 T by the linear relation $M(H, T) = M_s(T) + \chi(T)H$, where $M_s(T)$ is the saturation magnetization of the FeAs ferromagnetic impurity phase and $\chi(T)$ is the intrinsic magnetic susceptibility of the sample. At 100 K, the value of $M_s = 2.7 \times 10^{-2} \mu_B/\text{f.u.}$ corresponds to about 0.79 mol% MnAs impurities [$M_s = 3.40(3) \mu_B/\text{Mn}$ for MnAs at $T=0$ K].³⁶ Our $\chi(T)$ data in Fig. 7(a) are corrected for this ferromagnetic impurity contribution. We evidently could not completely correct for this ferromagnetic contribution since the corrected $\chi(T)$ still shows a small step at 300 K. This step is more pronounced in the $1/\chi$ plot. Our observations are in good agreement with those reported previously.²¹

Using the ionic model discussed above, χ_{core} was calculated to be $-1.68 \times 10^{-4} \text{ cm}^3/\text{mol}$ for $\text{Sr}_2\text{Mn}_3\text{As}_2\text{O}_2$. We fitted the $\chi(T)$ data from 130 K to 250 K in Fig. 7(a) by Eq. (1). The parameters χ_0 , C , and θ were found to be $-2.78(4) \times 10^{-3} \text{ cm}^3/\text{mol}$, $5.7(2) \text{ cm}^3 \text{ K/mol}$, and $-17(3) \text{ K}$, respectively. The fitted value of χ_0 is more negative than χ_{core} , which is unphysical since there are likely no other diamagnetic contributions to χ . Therefore in the following we fitted the data from 130 K to 250 K by fixing χ_0 to either zero or χ_{core} in Eq. (1). Setting $\chi_0 = 0$ yielded $C = 4.69(2) \text{ cm}^3 \text{ K/mol}$ and $\theta = 3(1) \text{ K}$, whereas setting $\chi_0 = \chi_{\text{core}}$ yielded $C = 4.75(2) \text{ cm}^3 \text{ K/mol}$ and $\theta = 1.5(7) \text{ K}$. Taking both values of C into consideration yields $\mu_{\text{eff}} = 6.14(2) \mu_B/\text{f.u.}$ This value is much smaller than the value of $10.3 \mu_B/\text{f.u.}$ expected for three paramagnetic Mn^{+2} spins per formula unit with $g = 2$ and $S = 5/2$. However, the MnAs sublattice within $\text{Sr}_2\text{Mn}_3\text{As}_2\text{O}_2$ undergoes long-range AF order at a Néel temperature $T_N = 340 \text{ K}$ with a G-type antiferromagnetic structure,²⁰ so only one out of the three Mn ions per formula unit (in the MnO_2 layer) should contribute to the Curie-Weiss law at lower T . Our value $\mu_{\text{eff}} = 6.14(2) \mu_B/\text{f.u.}$ deduced at 130 K to 250 K is indeed close to the value of $5.92 \mu_B$ expected for one spin $S = 5/2$ per formula unit with $g = 2$.

3. $\text{Sr}_2\text{Mn}_2\text{CuAs}_2\text{O}_2$

Magnetic Susceptibility Measurements

The molar $\chi(T)$ of $\text{Sr}_2\text{Mn}_2\text{CuAs}_2\text{O}_2$ in $H = 1 \text{ T}$ is shown in Fig. 8(a). Below about 125 K, $\chi(T)$ increases rapidly, suggesting the onset of ferrimagnetic/ferromagnetic ordering at a Curie temperature $T_C \sim 100 \text{ K}$ in contrast to the spin-glass type transitions evidently observed above for $\text{Sr}_2\text{Zn}_2\text{MnAs}_2\text{O}_2$

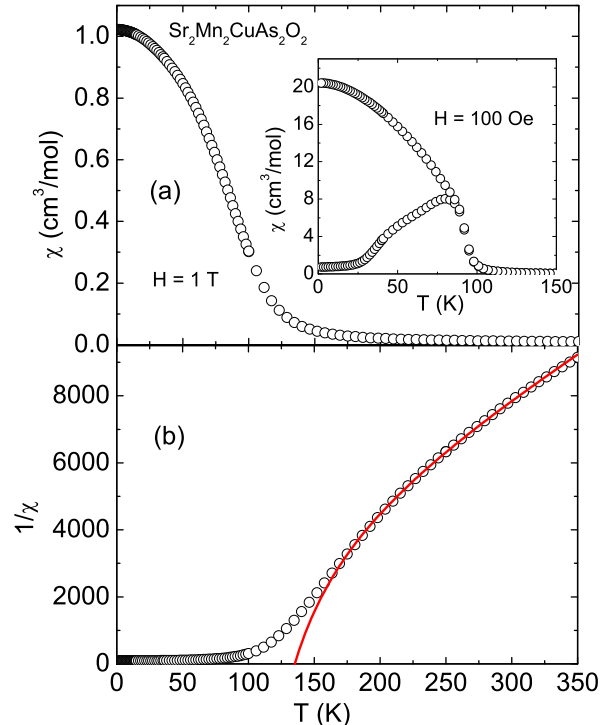


FIG. 8: (Color online) (a) Magnetic susceptibility of $\text{Sr}_2\text{Mn}_2\text{CuAs}_2\text{O}_2$ measured at $H = 1 \text{ T}$ versus temperature T . Inset shows ZFC and FC susceptibility versus T measured at $H = 100 \text{ Oe}$. (b) Inverse dimensionless volume susceptibility $1/\chi$ versus T . The solid curve is a fit to the $1/\chi$ data above 170 K by Eq. (4).

and $\text{Sr}_2\text{Mn}_3\text{As}_2\text{O}_2$. The ZFC and FC susceptibilities in $H = 100 \text{ Oe}$ show a significant splitting at 90 K as shown in the inset of Fig. 8(a). Such irreversibility is a characteristic behavior of ferrimagnetic/ferromagnetic compounds.³⁷ The magnetization isotherm data below confirm this interpretation.

Figure 8(b) shows $1/\chi$ versus T where in this case χ is the dimensionless volume susceptibility, which is the molar susceptibility divided by the molar volume V_M , both in units of cm^3/mol . We plot here the inverse volume susceptibility in order to fit the data later by theory. In the paramagnetic state ($T > T_c$), one would expect a linear T -dependence of $1/\chi$ due to local moments. Instead, we see a strong negative curvature. Fitting the data in Fig. 8 in different temperature ranges between 200 and 350 K by the Curie-Weiss behavior in Eq. (1) gave the large value $\chi_0 = 3.8(2) \times 10^{-3} \text{ cm}^3/\text{mol}$. For a metal, χ_0 has two contributions, the diamagnetic conduction electron Landau orbital susceptibility χ_L and the paramagnetic conduction electron Pauli spin susceptibility χ_P , in addition to the two contributions considered

above for insulators, so that

$$\chi_0 = \chi_{\text{core}} + \chi_{\text{VV}} + \chi_{\text{L}} + \chi_{\text{P}}. \quad (3)$$

For transition metal compounds, the magnitude of χ_{L} is small compared to χ_{VV} . A typical value for χ_{VV} is $\sim 1 \times 10^{-4} \text{ cm}^3$ per mole of transition metal atoms, which gives $\chi_{\text{VV}} \sim 3 \times 10^{-4} \text{ cm}^3$ per mole of $\text{Sr}_2\text{Mn}_2\text{CuAs}_2\text{O}_2$. Using the ionic model discussed above, we obtain $\chi_{\text{core}} = -1.65 \times 10^{-4} \text{ cm}^3/\text{mol}$. We estimate $\chi_{\text{P}} \sim 3 \times 10^{-4} \text{ cm}^3/\text{mol}$ obtained below from the heat capacity data analysis. Adding these contributions gives $\chi_0 \sim 4 \times 10^{-4} \text{ cm}^3/\text{mol}$. The above fitted value is an order of magnitude larger than this estimated χ_0 value and is hence unphysically large. Therefore we next considered a model in which the observed strong positive curvature in $\chi^{-1}(T)$ in Fig. 8(b) arises because the compound is a ferrimagnet.³⁸

From our neutron diffraction data below, we found that approximately equal amounts of Cu and Mn statistically occupy the metal atom positions in the *MA*s layers, and that only Mn occupies the metal atom positions in the *MO*₂ layers. One can therefore separate the magnetic atoms into A and B sublattices, where one of the sublattices is in the (Mn/Cu)As layer and the other sublattice is in the MnO₂ layer. From the crystal structure in Fig. 1, one would expect three distinct interactions between the Mn and Mn/Cu atoms: an interaction within each sublattice and an interaction between sublattices, such as mentioned in the context of molecular field theory in Ref. 38. However, having three interaction constants in addition to the unknown (average) Mn/Cu spin on one sublattice and Mn spin on the other sublattice as fitting parameters allows too many adjustable parameters in fitting the $\chi(T)$ data. Therefore, as an *effective* model, we set the intrasublattice (intralayer) interactions to zero and only consider bipartite interactions between magnetic atoms on the different A and B sublattices in adjacent layers. The physical motivation for this choice is that the adjacent Mn1 and Mn2/Cu2 layers will have distinctly different ordered moments/site and our model needs to differentiate these layers from each other.

In the molecular field approximation, the dimensionless volume susceptibility χ_{ferri} for such a ferrimagnet above its Curie temperature T_{C} is³⁸

$$\chi_{\text{ferri}} = \frac{(C_{\text{A}} + C_{\text{B}})T - 2T_{\text{C}}^2/\mu}{T^2 - T_{\text{C}}^2}, \quad (4)$$

where the ferrimagnetic Curie temperature is

$$T_{\text{C}} = \mu\sqrt{C_{\text{A}}C_{\text{B}}}, \quad (5)$$

μ is a positive (antiferromagnetic) dimensionless molecular field coupling constant between the two sublattices and C_{A} and C_{B} are the Curie constants per unit volume for sublattices A and B, respectively. The Curie constants and the saturation moment μ_{sat} per pair of A and B atoms are

$$C_{\text{A}} = \frac{N_{\text{A}}g^2\mu_{\text{B}}^2[S_{\text{A}}(S_{\text{A}} + 1)]}{3k_{\text{B}}(V_{\text{M}}/2)}, \quad (6)$$

$$C_{\text{B}} = \frac{N_{\text{A}}g^2\mu_{\text{B}}^2[S_{\text{B}}(S_{\text{B}} + 1)]}{3k_{\text{B}}(V_{\text{M}}/2)}, \quad (7)$$

$$\mu_{\text{sat}} = g\mu_{\text{B}}|S_{\text{A}} - S_{\text{B}}|, \quad (8)$$

where S_{A} and S_{B} are the spins of the atoms on the A and B sublattices (or average spin in the case of the Mn/Cu layer), respectively, $g = 2$ is the g -factor which we take to be the same for both magnetic species A and B, and $V_{\text{M}}/2$ is the volume per mole of A or B atoms which are assumed to be equal in number.

From our $M(H)$ measurements below, we obtain a reliable value for μ_{sat} , which allows us to eliminate one of the three variables μ , S_{A} and S_{B} (we choose to eliminate S_{A} and we take $g = 2$) as a fitting parameter in Eq. (4). Since χ_{ferri} in Eq. (4) is the dimensionless volume susceptibility, our experimental molar $\chi(T)$ data in Fig. 8(a) were converted to volume susceptibility by dividing by $V_{\text{M}} = N_{\text{A}}a^2c/4$ and were then plotted in Fig. 8(b) and fitted by Eq. (4) above 170 K. We fixed $\mu_{\text{sat}} = 2.20 \mu_{\text{B}}/\text{f.u.}$ as obtained from an $M(H)$ measurement at 1.8 K (see Fig. 9 below). We first fitted the data by $\chi = \chi_0 + \chi_{\text{ferri}}$ and obtained the parameters $\chi_0 = 1.06(7) \times 10^{-5}$ (which is equal to $0.99(7) \times 10^{-3} \text{ cm}^3/\text{mol}$), $S_{\text{B}} = 0.26(1)$ and $\mu = 12600(300)$, which gives $T_{\text{C}} = 138(4)$ K. Using the value of S_{B} in Eq. (8), S_{A} was calculated to be 1.36(1). Thus the saturation moments per formula unit on layers B and A are

$$\mu_{\text{sat}} = 0.52 \mu_{\text{B}}/\text{B layer} \quad (\chi_0 \neq 0) \quad (9)$$

$$\mu_{\text{sat}} = 2.72 \mu_{\text{B}}/\text{A layer}.$$

In the ferrimagnetically-ordered state, these are antiparallel, giving a net saturation moment of $\mu = \mu_{\text{A atom}} - \mu_{\text{B atom}} = 2.20 \mu_{\text{B}}/\text{f.u.}$, by construction. The χ_0 value is somewhat larger than expected. Therefore we carried out another fit by setting $\chi_0 = 0$ and the resultant fitting parameters were $S_{\text{B}} = 0.35(1)$, $\mu = 9840(40)$, which gives $T_{\text{C}} = 137(1)$ K. From Eq. (8), S_{A} was calculated to be 1.45(1). In this case, we have the saturation moments per formula unit

$$\mu_{\text{sat}} = 0.70 \mu_{\text{B}}/\text{B layer} \quad (\chi_0 = 0) \quad (10)$$

$$\mu_{\text{sat}} = 2.90 \mu_{\text{B}}/\text{A layer}.$$

Due to the highly simplified model, the saturation moments in Eqs. (9) and (10) should be considered to be semiquantitative only. Indeed, from the results of the magnetic structure refinement by neutron diffraction in Table VI below, the Mn2 layer has $\mu_{\text{sat}} = 2.2 \mu_{\text{B}}/\text{f.u.}$ and the Mn1 layer has $\mu_{\text{sat}} = 3.9 \mu_{\text{B}}/\text{f.u.}$

We assume a Heisenberg exchange interaction between the sublattice A and B spins given by the Hamiltonian $\mathcal{H} = J \sum_{\langle ij \rangle} \vec{S}_i \cdot \vec{S}_j$, where the sum is over nearest-neighbor A and B spin pairs. We estimate the nearest-neighbor antiferromagnetic A-B exchange coupling J

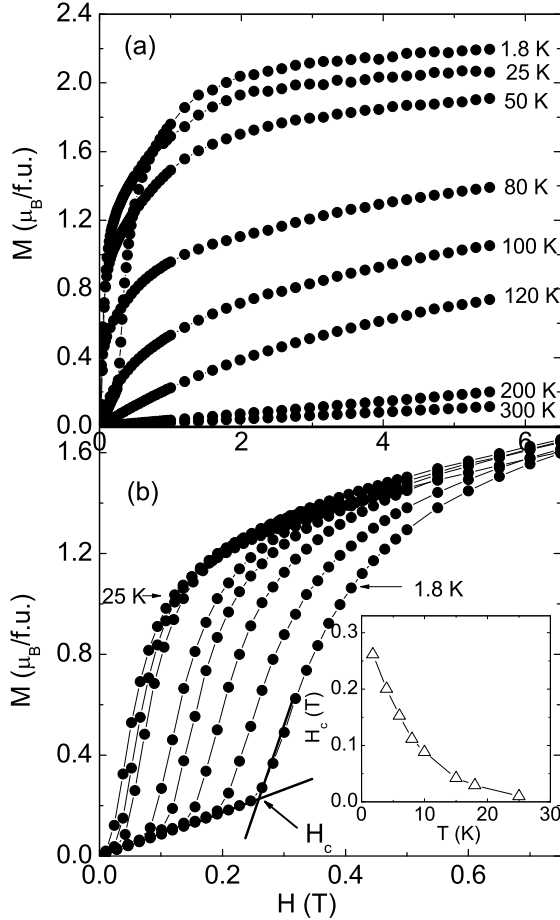


FIG. 9: (a) Magnetization M versus field H isotherms for $\text{Sr}_2\text{Mn}_2\text{CuAs}_2\text{O}_2$ at the indicated temperatures. (b) Low temperature $M(H)$ at low T and H . The construction used to determine the metamagnetic critical field H_c is indicated. Inset: H_c versus T .

from the molecular field coupling constant μ using³⁸

$$\mu = \frac{Jz\Omega}{g^2\mu_B^2}, \quad (11)$$

where $\Omega = (V_M/2)/N_A$ is the volume per spin and $z = 8$ is the number of nearest neighbor spins in the opposite sublattice in the two adjacent layers (see Fig. 1). Using the above values of μ yields $J/k_B = 90(11)$ K.

Magnetization versus Applied Magnetic Field Measurements

Figure 9 shows $M(H)$ isotherms at different temperatures for $\text{Sr}_2\text{Mn}_2\text{CuAs}_2\text{O}_2$ measured up to $H = 5.5$ T. At 300 K M is proportional to H but below 150 K $M(H)$ begins to show saturation. At the lowest temperature of 1.8 K, M almost saturates at 5 T and the

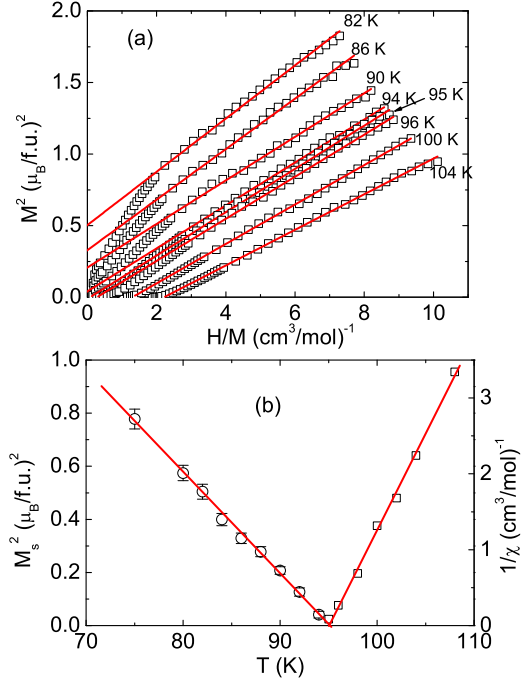


FIG. 10: (Color online) (a) Arrott plots of the square of the magnetization M^2 versus the ratio of the applied magnetic field to the magnetization H/M for $\text{Sr}_2\text{Mn}_2\text{CuAs}_2\text{O}_2$ at representative temperatures T near T_C . The solid red lines are linear fits to the data for $H \geq 1$ T and are extrapolated to $H/M = 0$. (b) Square of the spontaneous magnetization M_s^2 (left-hand scale) and the inverse of the intrinsic zero-field magnetic susceptibility $1/\chi$ (right-hand axis) versus T , derived from the fits in (a). The solid red lines are linear fits to the respective data.

saturation moment is $\mu_{\text{sat}} \approx 2.2 \mu_B/\text{f.u.}$ if one assumes that M saturates at high fields. If one instead assumes a linear behavior at high fields and extrapolates the high field $M(H)$ to $H = 0$, one obtains a slightly lower value $\mu_{\text{sat}} \approx 2.0 \mu_B/\text{f.u.}$ These data suggest that $\text{Sr}_2\text{Mn}_2\text{CuAs}_2\text{O}_2$ is a ferromagnet or ferrimagnet in contrast to $\text{Sr}_2\text{Zn}_2\text{MnAs}_2\text{O}_2$ which shows spin-glass ordering. As shown in Fig. 9(b), $M(H)$ for $\text{Sr}_2\text{Mn}_2\text{CuAs}_2\text{O}_2$ at 1.8 K shows a pronounced step at about 3 kOe pointing towards a spin-flop type metamagnetic transition at a critical field H_c . As shown in the inset of Fig. 9(b), H_c decreases with increasing T and is completely suppressed at 25 K, which is far below the Curie temperature T_C . Since the material is a ferrimagnet H_c may therefore be associated with domain wall depinning.

In order to further study the magnetic behavior, we measured $M(H)$ isotherms in the vicinity of T_C . With the help of Arrott plots³⁹ in which the square of the magnetization M^2 in an applied field H is plotted as a function of H/M for fixed temperatures T , we estimated T_C . This is a very useful and standard method for estab-

lishing the presence of ferromagnetic/ferrimagnetic order and also for an accurate determination of T_C . This approach is based on the Weiss molecular-field theory which predicts that such plots yield straight line isotherms with an intercept which tends to zero as T approaches T_C from above. However experimentally such Arrott plots can exhibit considerable curvature arising from non-mean-field behavior. Therefore generalized Arrott plots have been used where $M^{1/\beta}$ is plotted against $(H/M)^{1/\gamma}$.^{40–42} Based on the values of the critical exponents β and γ values that give linear plots, the universality class of the magnetic system can be inferred.

Figure 10(a) shows Arrott plots of M^2 vs H/M near T_C for $\text{Sr}_2\text{Mn}_2\text{CuAs}_2\text{O}_2$. The data are well fitted by linear behaviors for fields higher than 1 T. Data at low fields are ignored in such plots because those data can be unduly affected by a small fraction of the sample. For $T > T_C$ one has

$$M^2(T) = A(T) \left[\frac{H}{M(H,T)} - \frac{1}{\chi(T)} \right], \quad (T > T_C) \quad (12)$$

from which one can infer the inverse of the intrinsic zero-field susceptibility $\chi^{-1}(T)$ as the intercept on the horizontal H/M axis as shown in Fig. 10(b) (right-hand axis). A linear extrapolation of the $1/\chi$ data to $1/\chi = 0$ gives $T_C = 95.1(2)$ K. Fitting the $\chi^{-1}(T)$ data in Fig. 10(b) by a Curie-Weiss law gives the Curie constant and effective moment as

$$\begin{aligned} C &= 3.86(9) \text{ cm}^3 \text{ K/mol} \\ \mu_{\text{eff}} &= 5.55(6) \mu_B/\text{f.u.} \end{aligned} \quad (13)$$

Anticipating the results of the magnetic structure refinement by neutron diffraction in Table VI below, we have one Mn1 spin $S = 2$ and two Mn2 *site* spins $S = 1/2$ per formula unit, giving an effective moment of $5.48 \mu_B/\text{f.u.}$ assuming $g = 2$, in excellent agreement with the value in Eq. (13).

For $T < T_C$, one has

$$M^2(T) = M_s^2(T) + A \frac{H}{M}, \quad (T < T_C), \quad (14)$$

from which one can infer the square of the spontaneous magnetization $M_s^2(T)$ from the intersection of the fitted line with the vertical M^2 axis as shown in Fig. 10(b) (left-hand axis). The susceptibility at $T > T_C$ and saturation magnetization at $T < T_C$ of a ferrimagnet or ferromagnet are expected to follow critical behaviors $1/\chi = (T/T_C - 1)^\gamma$ and $M_s \sim (1 - T/T_C)^\beta$, respectively.⁴² As shown in Fig. 10(b), M_s^2 versus T is linear indicating that the critical exponent $\beta \approx 0.50$ and the linear T -dependence of $1/\chi$ gives $\gamma = 1$ which are both consistent with the predictions of mean-field theory.⁴⁰ From these results $\text{Sr}_2\text{Mn}_2\text{CuAs}_2\text{O}_2$ appears to be a good example of a mean-field ferrimagnet. Therefore, it is very surprising that there is no discernable heat capacity anomaly associated with the transition at $T_C = 95$ K [see Fig. 10(b)], as shown in the next section.

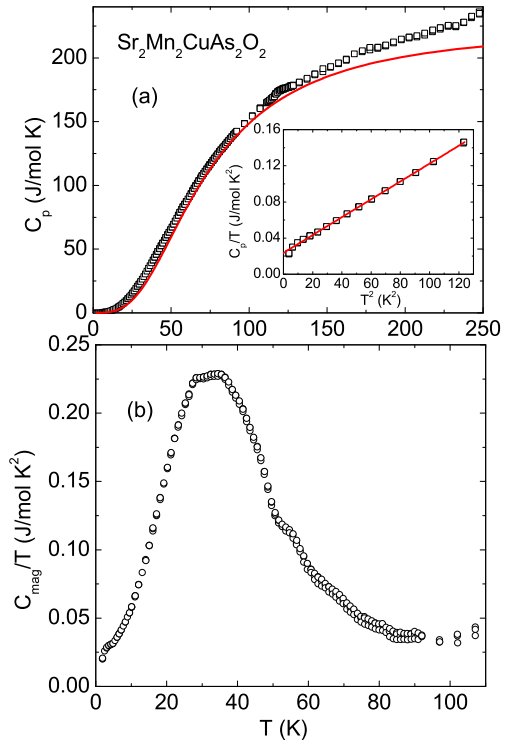


FIG. 11: (Color online) (a) Heat capacity C_p versus temperature T for $\text{Sr}_2\text{Mn}_2\text{CuAs}_2\text{O}_2$. The solid red curve is a fit of the Debye function to the data around 100 K which is taken as an approximation to the lattice heat capacity. Inset: C_p/T vs. T^2 below 11 K. The red line is a linear fit to the data from 1.8 to 11 K. (b) Magnetic contribution to the heat capacity divided by temperature, C_{mag}/T , versus T .

TABLE IV: Linear specific heat coefficients A and Debye temperatures Θ_D for $\text{Sr}_2\text{Mn}_3\text{As}_2\text{O}_2$, $\text{Sr}_2\text{Zn}_2\text{MnAs}_2\text{O}_2$ and $\text{Sr}_2\text{Mn}_3\text{As}_2\text{O}_2$ obtained from fitting the low-temperature specific heat data by Eq. (15). The large A value for $\text{Sr}_2\text{Zn}_2\text{MnAs}_2\text{O}_2$ may not be the low- T limit because $C(T)$ for this sample showed a sharp downturn below 4 K.

Compound	A (mJ/mol K ²)	Θ_D (K)
$\text{Sr}_2\text{Mn}_2\text{CuAs}_2\text{O}_2$	23.6(3)	260(1)
$\text{Sr}_2\text{Zn}_2\text{MnAs}_2\text{O}_2$	73.0(4)	252(1)
$\text{Sr}_2\text{Mn}_3\text{As}_2\text{O}_2$	13.1(3)	263(1)

D. Heat Capacity Measurements

The heat capacity at constant pressure C_p at $H = 0$ is plotted versus T in Figs. 11(a), 12(a), and 13 for $\text{Sr}_2\text{Mn}_2\text{CuAs}_2\text{O}_2$, $\text{Sr}_2\text{Zn}_2\text{MnAs}_2\text{O}_2$, and $\text{Sr}_2\text{Mn}_3\text{As}_2\text{O}_2$, respectively. The values of C_p at room 250 K are about 240 and 225 J/mol K for $\text{Sr}_2\text{Mn}_2\text{CuAs}_2\text{O}_2$ and

$\text{Sr}_2\text{Zn}_2\text{MnAs}_2\text{O}_2$, respectively. These values are comparable with the Dulong-Petit classical lattice heat capacity at constant volume $C_V = 27R = 225 \text{ J/mol K}$.³⁸ The observed value that is somewhat larger than the Dulong-Petit value may be due to the fact that the compound is measured at constant pressure rather than constant volume and/or to a significant magnetic contribution being present in addition to the lattice contribution.

1. $\text{Sr}_2\text{Mn}_2\text{CuAs}_2\text{O}_2$

As shown in the inset of Fig. 11(a) $C_p(T)/T$ versus T^2 for $\text{Sr}_2\text{Mn}_2\text{CuAs}_2\text{O}_2$ is almost linear at low temperatures ($2 \text{ K} \leq T \leq 11 \text{ K}$). The resistivity data for this compound in Fig. 3 suggested a metallic ground state, so we fitted the data at low temperatures by the expression

$$\frac{C_p(T)}{T} = A + \beta T^2, \quad (15)$$

where the first term is interpreted for this sample as the Sommerfeld electronic specific heat coefficient due to conduction electrons and the second term is the low-temperature limit of the lattice heat capacity. The resultant A value is listed in Table IV.

From the value of β one can estimate the Debye temperature Θ_D using the expression³⁸

$$\Theta_D = \left(\frac{12\pi^4 R n}{5\beta} \right)^{1/3}, \quad (16)$$

where R is the molar gas constant and n is the number of atoms per formula unit ($n = 9$ for our compounds). The β value yields the value of Θ_D listed in Table IV.

The density of states at the Fermi energy for both spin directions $N(E_F)$ can be estimated from the value of A using the relation³⁸

$$A = \frac{\pi^2}{3} k_B^2 N(E_F) (1 + \lambda_{ep}) \quad (17)$$

where λ_{ep} is the electron-phonon coupling constant. As a first approximation we set $\lambda_{ep} = 0$, which gives $N(E_F) \simeq 10.0 \text{ states/(eV f.u.)}$. From $N(E_F)$ we calculated the Pauli spin susceptibility χ_P using³⁸

$$\chi_P = \mu_B^2 N(E_F) \quad (18)$$

where μ_B is the Bohr magneton. This gives $\chi_P \simeq 3.24 \times 10^{-4} \text{ cm}^3/\text{mol}$.

2. $\text{Sr}_2\text{Zn}_2\text{MnAs}_2\text{O}_2$ and $\text{Sr}_2\text{Mn}_3\text{As}_2\text{O}_2$

For $\text{Sr}_2\text{Zn}_2\text{MnAs}_2\text{O}_2$, $C_p(T)/T$ versus T^2 shows a sharp decrease below about 4 K but a linear region was observed just above this temperature ($4 \text{ K} \leq T \leq 14 \text{ K}$) [inset of Fig. 12(a)]. For $\text{Sr}_2\text{Mn}_3\text{As}_2\text{O}_2$ which is also an insulator, $C_p(T)/T$ versus T^2 is almost linear from

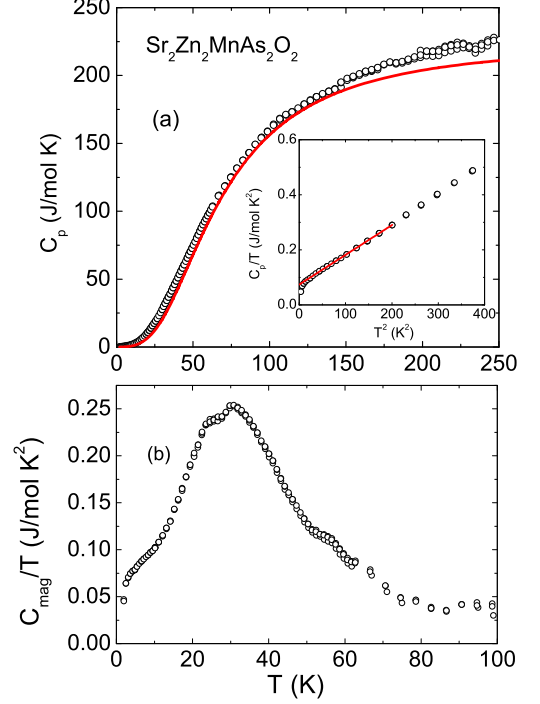


FIG. 12: (Color online) (a) Heat capacity C_p versus temperature T for $\text{Sr}_2\text{Zn}_2\text{MnAs}_2\text{O}_2$. The solid red curve is a fit of the Debye function to the data around 100 K which is taken as an approximation to the lattice heat capacity. Inset: C_p/T vs. T^2 below 20 K. The red line is a linear fit to the data from 4 to 14 K. The data below 4 K show a sharp decrease. The data start to deviate from linear behavior above 14 K. (b) Magnetic contribution to the heat capacity divided by temperature, C_{mag}/T , versus T .

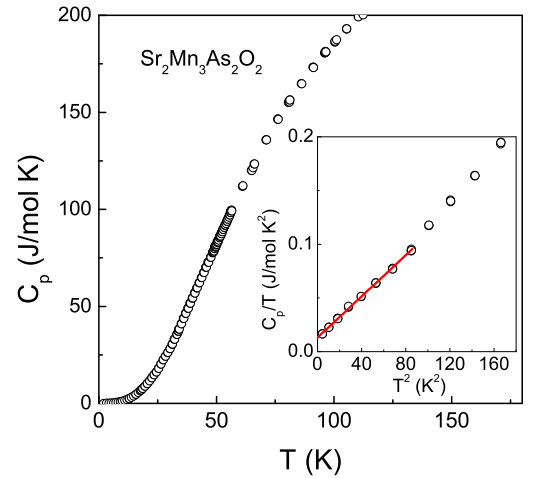


FIG. 13: (Color online) Heat capacity C_p vs. temperature T for $\text{Sr}_2\text{Mn}_3\text{As}_2\text{O}_2$. Inset: C_p/T vs. T^2 . The solid red line is a linear fit from 1.8 to 9 K.

our low temperature limit of 2 K up to 9 K (inset of Fig. 13). To parametrize the data, we fitted the $C_p(T)/T$ vs. T^2 data in these linear regimes by Eq. (15). The parameters obtained from the fits are shown in Table IV. For these compounds, since the $\rho(T)$ measurements indicated insulating ground states, the A values may be related to the spin-glass like behavior observed in $\chi(T)$.⁴⁵ In $\text{Sr}_2\text{Mn}_3\text{As}_2\text{O}_2$, since the MnAs sublattice orders at 340 K, in the ordered state the magnetic part of the heat capacity may contain a T^3 term due to spin-wave excitations, and our experimental β would then have a contribution from the spin-wave excitations. Thus our estimated Θ_D gives a lower limit of the Debye temperature in $\text{Sr}_2\text{Mn}_3\text{As}_2\text{O}_2$. These estimated Θ_D values are much higher than that reported for $\text{Ba}_2\text{Zn}_2\text{MnAs}_2\text{O}_2$ ($\Theta_D = 111$ K)⁴⁵ but are comparable to those for BaMn_2As_2 (Refs. 34 and 46) and $(\text{Ba,Sr})\text{Ru}_2\text{As}_2$.⁴⁷

3. Magnetic Heat Capacity Contributions

In an attempt to extract the magnetic heat capacity $C_{\text{mag}}(T)$ from the observed data, we approximate the lattice contribution $C_{\text{latt}}(T)$ by the Debye function³⁸

$$C_{\text{latt}}(T) = 9R \left(\frac{T}{\Theta_D} \right)^3 \int_0^{\Theta_D/T} \frac{x^4 e^x}{(e^x - 1)} dx. \quad (19)$$

The solid curves in Figs. 11(a) and 12(a) are plots of $C_{\text{latt}}(T)$ obtained by fitting the high temperature data, yielding $\Theta_D = 300$ K and 280 K for $\text{Sr}_2\text{Mn}_2\text{CuAs}_2\text{O}_2$ and $\text{Sr}_2\text{Zn}_2\text{MnAs}_2\text{O}_2$, respectively. These Θ_D values are somewhat larger than the values in Table IV estimated from our *low*-temperature heat capacity measurements. The magnetic contribution $C_{\text{mag}}(T)$ is obtained by subtracting the respective calculated lattice contribution from the observed data. The resulting $C_{\text{mag}}(T)/T$ is plotted versus T in Figs. 11(b) and 12(b), respectively. We did not observe any clear anomaly in $C_{\text{mag}}(T)$ associated with any magnetic transition as inferred from the above $\chi(T)$ measurements. The magnetic entropies $S_{\text{mag}}(T) = \int_{1.8\text{K}}^T [C_{\text{mag}}(T')/T'] dT'$ at $T = 100$ K are 5.05 and 11 J/(mol Mn K) for $\text{Sr}_2\text{Mn}_2\text{CuAs}_2\text{O}_2$ and $\text{Sr}_2\text{Zn}_2\text{MnAs}_2\text{O}_2$, respectively.

We were not able to fit the high- T $C_p(T)$ data for $\text{Sr}_2\text{Mn}_3\text{As}_2\text{O}_2$ adequately by Eq. (19). This may be due to the magnetic ordering of the MnAs sublattice at 340 K which could have a significant magnetic contribution thereby enhancing the total C_p at high temperatures.

From the neutron diffraction solution of the combined crystallographic and magnetic structures at 4 K for $\text{Sr}_2\text{Mn}_2\text{CuAs}_2\text{O}_2$ in Table VI below, the $n_1 = 1$ Mn1 atoms/f.u. have ordered moments of $3.89(11) \mu_B/\text{Mn}$ corresponding to spin $S_1 = 2$ with $g = 2$, and each of the $n_2 = 2$ Mn2 sites/f.u. has a magnetic moment of $1.10(7) \mu_B/\text{Mn}$ corresponding to spin $S_2 = 1/2$. Therefore the entropy of the disordered spins at high temper-

atures is calculated to be

$$S_{\text{calc}} = \sum_{i=1}^2 n_i R \ln(2S_i + 1) = 3.00R = 24.9 \frac{\text{J}}{\text{mol K}}, \quad (20)$$

where R is the molar gas constant. This is much larger than the value of 10.1 J/mol K at 100 K estimated above for the magnetic component of the heat capacity. Similarly, for $\text{Sr}_2\text{Zn}_2\text{MnAs}_2\text{O}_2$, if we assume a spin between 2 and 5/2 for the Mn, the predicted disordered entropy is between 13.4 and 14.9 J/mol K, which is again somewhat larger than the value $S_{\text{mag}} = 11$ J/(mol K) inferred above. These discrepancies likely result from inaccurate estimates of the respective lattice heat capacities that were used to obtain the magnetic heat capacity from the observed values. It would be useful to synthesize and measure the heat capacity of a nonmagnetic reference compound to obtain a better estimate of the lattice heat capacity versus temperature.

E. Neutron Powder Diffraction Measurements

Neutron powder diffraction measurements were undertaken to answer two key questions regarding the $\text{Sr}_2\text{Mn}_2\text{CuAs}_2\text{O}_2$ compound. First, it is important to identify the site(s) in the lattice occupied by the Cu. The large difference between the coherent scattering lengths⁴⁴ b_{coh} for Mn ($b_{\text{coh}} = -3.75$ fm) and Cu ($b_{\text{coh}} = 7.72$ fm) provides excellent contrast for this purpose. Second, as described above, magnetization measurements suggest that $\text{Sr}_2\text{Mn}_2\text{CuAs}_2\text{O}_2$ is ferrimagnetic, in contrast to the G-type antiferromagnetic ordering found for Mn2 in $\text{Sr}_2\text{Mn}_3\text{As}_2\text{O}_2$, where the two members of all nearest neighbor spin pairs are antiparallel. In addition, we carried out measurements on a powder sample of $\text{Sr}_2\text{Mn}_3\text{As}_2\text{O}_2$ for comparison with previous work and with our data for $\text{Sr}_2\text{Mn}_2\text{CuAs}_2\text{O}_2$. The microscopic details of the magnetic structure of $\text{Sr}_2\text{Mn}_2\text{CuAs}_2\text{O}_2$, and how it differs from the $\text{Sr}_2\text{Mn}_3\text{As}_2\text{O}_2$ parent compound are, again, best probed by neutron diffraction.

1. $\text{Sr}_2\text{Mn}_3\text{As}_2\text{O}_2$

In Fig. 14(a) we plot the neutron diffraction data at temperature $T = 4$ K, along with the fit that results from the refinement that includes the crystallographic and G-type magnetic structure as well as a small amount (2–3%) of MnO impurity phase. The crystallographic parameters from our refinements of $\text{Sr}_2\text{Mn}_3\text{As}_2\text{O}_2$ are listed in Table V. The error estimates in this table represent only the statistical errors associated with the refinement itself. Consistent with previous work, we found no significant changes in crystal structure with temperature.

Focusing now on the magnetic structure, in Fig. 15(a) we show that as temperature is decreased below 300 K the intensity of the (101) diffraction peak increases, while

TABLE V: Crystallographic and magnetic neutron powder diffraction refinement data for $\text{Sr}_2\text{Mn}_3\text{As}_2\text{O}_2$, body-centered-tetragonal, space group $I4/mmm$ (No. 139), $Z = 2$ formula units/unit cell. The Mn1 atoms are in MnO_2 layers and the Mn2 atoms are in Mn_2As_2 layers.

T	375 K	300 K	150 K	4 K
a (Å)	4.14453(2)	4.14079(4)	4.13438(3)	4.13104(4)
c (Å)	18.8530(1)	18.8217(2)	18.7672(1)	18.7382(2)
Unit cell volume (Å ³)	323.841(3)	322.721(5)	320.789(4)	319.776(6)
Sr in $4e$ (0 0 z)				
z	0.41379(6)	0.41362(6)	0.41358(6)	0.41358(7)
B_{iso}	0.81(2)	0.68(6)	0.34(3)	0.26(3)
Mn1 in $2a$ (0 0 0)				
B_{iso}	0.82(6)	0.78(4)	0.47(5)	0.33(7)
Ordered moment ($\mu_{\text{B}}/\text{Mn1}$)	—	—	0	?
Mn2 in $4d$ (0 1/2 1/4)				
B_{iso}	0.99(4)	0.40(5)	0.41(4)	0.36(4)
Ordered moment ($\mu_{\text{B}}/\text{Mn2}$)	—	2.10(3)	3.18(3)	3.50(4)
As in $4e$ (0 0 z)				
z	0.16900(7)	0.16892(7)	0.16893(6)	0.16894(8)
B_{iso}	0.80(2)	0.61(3)	0.30(3)	0.26(3)
O in $4c$ (0 1/2 0)				
B_{iso}	1.01(3)	0.89(3)	0.55(3)	0.43(3)
R_{Bragg} (%)	5.35	4.87	4.37	4.78
R_{Magnetic} (%)	—	4.38	2.77	3.1
χ^2	1.71	1.89	2.54	5.41

the intensity of the (110) peak remains constant, again consistent with the G-type antiferromagnetic ordering of the Mn2 site as described previously,²⁰ and illustrated in Fig. 16(a). The ordered moment at our base temperature of 4 K is 3.50(4) μ_{B} per Mn2 ion.

As shown in the inset of Fig. 14(a), at 4 K we also find evidence of a change in the magnetic structure with the appearance of a new peak, identified by Brock et al. as the (100) reflection associated with the magnetic unit cell described by $a_{\text{mag}} = \sqrt{2}a$ and $c_{\text{mag}} = c$ for $\text{Sr}_2\text{Mn}_3\text{As}_2\text{O}_2$. The new magnetic peak was previously assigned to a quasi-2D-ordering of the Mn1 sublattice.²⁰ However, we observed no additional reflections at the expected higher index positions [e.g. (110)_{mag} and (112)_{mag}]. Since no model was found to fully explain the observed scattering data, the above refinement of the magnetic structure at 4 K was conducted by excluding the data points associated with the new peak. Single crystal neutron measurements would be useful to resolve the nature of this additional reflection and its relationship to the magnetic structure at low temperature.

2. $\text{Sr}_2\text{Mn}_2\text{CuAs}_2\text{O}_2$

Moving now to the $\text{Sr}_2\text{Mn}_2\text{CuAs}_2\text{O}_2$ sample, Fig. 14(b) and Table VI describe the results of our refinements of the crystallographic and magnetic structures of this com-

pound. Similar to what was found for $\text{Sr}_2\text{Mn}_3\text{As}_2\text{O}_2$, the diffraction pattern indicates the presence of MnO but, in addition, a small amount of a second phase that could not be identified also appears. Nevertheless, a reasonable refinement of the crystallographic and magnetic phase parameters was obtained. As Table VI shows, the most striking result of the crystallographic refinement is that the Cu is found only in the Mn2 site, associated with the Mn_2As_2 layers in the structure. Attempts to substitute Cu in the Mn1 sites resulted in significantly poorer refinement R -factors. We further note that, given the stoichiometry of the sample, the Cu occupancy on the Mn2 site is somewhat lower than the nominal value (37% vs. 50%), but this decrease may be associated with the presence of the second impurity phase in this sample.

Finally, we turn to the results of the refinement of the magnetic structure of $\text{Sr}_2\text{Mn}_2\text{CuAs}_2\text{O}_2$. Figure 14(b) clearly indicates some differences in magnetic behavior as compared to the parent $\text{Sr}_2\text{Mn}_3\text{As}_2\text{O}_2$ compound. First, the transition temperature is reduced from approximately 340 K (Ref. 20) to below 150 K. Second, we see from Fig. 15(b) that the intensities of both the (101) and (110) reflections increase below the magnetic transition in contrast to what is found for $\text{Sr}_2\text{Mn}_3\text{As}_2\text{O}_2$ in Fig. 15(a). The results of the refinement of the magnetic structure at $T = 60$ K and $T = 4$ K are given in Table VI and illustrated in Fig. 16(b). Consistent with the results of the bulk magnetization and magnetic suscep-

TABLE VI: Crystallographic and magnetic neutron powder diffraction refinement data for $\text{Sr}_2\text{Mn}_2\text{CuAs}_2\text{O}_2$, body-centered-tetragonal, space group $I4/mmm$ (No. 139), $Z = 2$ formula units/unit cell. The Mn1 atoms are in MnO_2 layers and the Mn2/Cu atoms are in $(\text{Mn}/\text{Cu})_2\text{As}_2$ layers.

T	300 K	120 K	60 K	4 K
a (Å)	4.07913(6)	4.07198(5)	4.07086(5)	4.07106(5)
c (Å)	18.5826(3)	18.5216(2)	18.4861(2)	18.4784(2)
Unit cell volume (Å ³)	309.201(8)	307.108(7)	306.351(7)	306.253(7)
Sr in $4e$ (0 0 z)				
z	0.4094(1)	0.40933(9)	0.40932(9)	0.40913(9)
B_{iso}	0.57(4)	0.32(4)	0.16(3)	0.10(3)
Mn1 in $2a$ (0 0 0)				
B_{iso}	0.62(9)	0.37(8)	0.16(8)	0.13(8)
Ordered moment ($\mu_{\text{B}}/\text{Mn1}$)	—	—	2.98(13)	3.89(11)
Mn2/Cu in $4d$ (0 1/2 1/4)				
Cu occupancy	37(1)%	37%	37%	37%
B_{iso}	0.65(5)	0.40(5)	0.22(5)	0.16(5)
Ordered moment ($\mu_{\text{B}}/\text{Mn2 site}$) ^a	—	—	0.91(10)	1.10(7)
Ordered moment ($\mu_{\text{B}}/\text{Mn2 atom}$) ^b	—	—	1.43(17)	1.72(13)
As in $4e$ (0 0 z)				
z	0.1684(1)	0.1683(1)	0.1684(1)	0.1684(1)
B_{iso}	0.58(4)	0.35(4)	0.23(4)	0.26(4)
O in $4c$ (0 1/2 0)				
B_{iso}	0.91(5)	0.64(5)	0.53(5)	0.47(5)
R_{Bragg} (%)	6.04	5.23	5.81	5.38
R_{Magnetic} (%)	—	—	12.4	10.3
χ^2	2.37	2.80	2.65	3.28

^aMeasured.

^bInferred from the 63% occupation of the Mn2 sites by Mn and 37% by nonmagnetic Cu.

tibility measurements, we find a ferrimagnetic structure with a net moment on the MnO_2 planes (Mn1 site) that is oriented antiparallel to the net moment in the Mn_2As_2 planes (Mn2 site). Thus there is a dramatic change in the magnetic structure. The magnetic structure has changed from a G-type antiferromagnet to an A-type ferrimagnet, where the spins within a layer are ferromagnetically aligned with each other, but adjacent ferromagnetic layers are antiferromagnetically aligned. The ferrimagnetic state arises instead of an antiferromagnetic state because the opposing spins in adjacent layers do not have the same magnitude per formula unit.

At $T = 4$ K, the ordered moment on the Mn1 site is $3.89(11) \mu_{\text{B}}/\text{Mn1}$ atom (or per Mn1 site since the Mn1 site is fully occupied by Mn), whereas the average moment per Mn2 site is reduced to $1.10(7) \mu_{\text{B}}/\text{Mn1}$ site. Thus the ordered moments per formula unit in the Mn_2As_2 and MnO_2 layers are

$$\begin{aligned} \mu_{\text{Mn}_2\text{As}_2} &= 2[1.10(7)] = 2.20(14) \mu_{\text{B}} \\ &\quad \text{(neutron diffraction)} \quad (21) \\ \mu_{\text{MnO}_2} &= 3.89(11) \mu_{\text{B}}. \end{aligned}$$

These values are significantly larger in magnitude than

estimated in Eqs. (9) and (10) from a fit to the $\chi(T)$, but this disagreement is not too surprising in view of the crude model used to fit the susceptibility data to obtain the latter two sets of values. The net ferrimagnetic moment at $T = 4$ K from our neutron diffraction structure refinement is $\mu_{\text{sat}} = 3.89(11) - 2.20(14) = 1.7(3) \mu_{\text{B}}/\text{f.u.}$, which is reasonably close to the saturation moment $\mu_{\text{sat}} = 2.0 \mu_{\text{B}}/\text{f.u.}$ extrapolated to zero field from the $M(H)$ measurements at 1.8 K in Fig. 9. Similar to $\text{Sr}_2\text{Mn}_3\text{As}_2\text{O}_2$, $\text{Sr}_2\text{Mn}_2\text{CuAs}_2\text{O}_2$ does not exhibit any clear additional three-dimensional long-range magnetic ordering transitions below the initial ordering temperature.

IV. DISCUSSION

The effective moments μ_{eff} for $\text{Sr}_2\text{Zn}_2\text{MnAs}_2\text{O}_2$ [$5.57(5) \mu_{\text{B}}/\text{f.u.}$ from Fig. 5] and $\text{Sr}_2\text{Mn}_3\text{As}_2\text{O}_2$ [$6.14(2) \mu_{\text{B}}/\text{f.u.}$ from Fig. 7(a)] are close to the spin-only value of $5.92 \mu_{\text{B}}$ expected for the high spin state ($S = 5/2$) of Mn^{2+} with $g = 2$. In $\text{Sr}_2\text{Mn}_3\text{As}_2\text{O}_2$ this value is attributed to the single disordered Mn/f.u. below

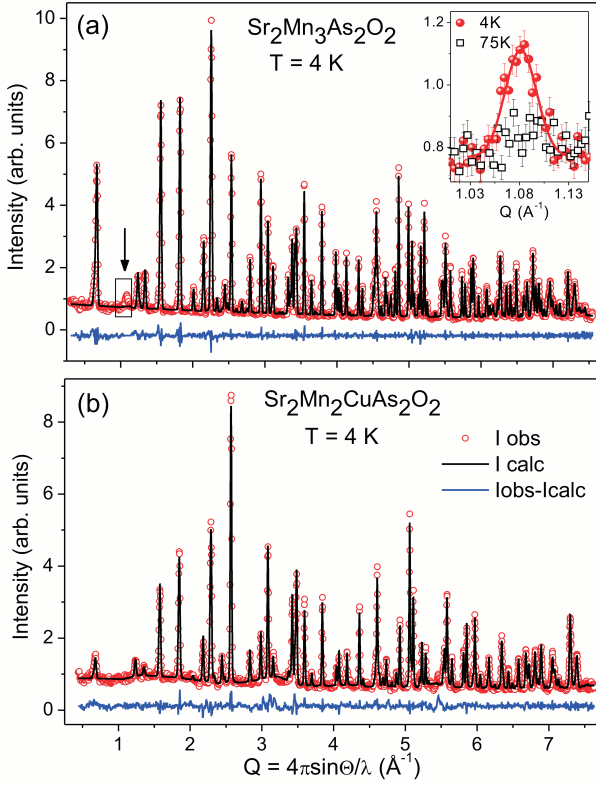


FIG. 14: (Color online) Neutron diffraction data collected at temperature $T = 4$ K (open circles) and calculated profiles (solid line) for (a) $\text{Sr}_2\text{Mn}_3\text{As}_2\text{O}_2$ and (b) $\text{Sr}_2\text{Mn}_2\text{CuAs}_2\text{O}_2$. The difference between observed and calculated profiles is shown at the bottom of each panel. The inset in (a) displays the $(100)_{\text{mag}}$ magnetic peak which appears below 75 K for $\text{Sr}_2\text{Mn}_3\text{As}_2\text{O}_2$. The position of this peak is indicated by the vertical arrow located towards the left in the main figure.

the Néel temperature $T_N = 340$ K at which the other two Mn/f.u. exhibit long-range antiferromagnetic order. The Weiss temperatures in the Curie-Weiss law are $+42(2)$ K for $\text{Sr}_2\text{Zn}_2\text{MnAs}_2\text{O}_2$ and $+3(1)$ K for $\text{Sr}_2\text{Mn}_3\text{As}_2\text{O}_2$. The $\chi(T)$ data show a bifurcation between the FC and ZFC data at about 50 K in both compounds. The $M(H)$ data for $\text{Sr}_2\text{Zn}_2\text{MnAs}_2\text{O}_2$ show no evidence for ferromagnetic ordering. The combination of these data and the $\chi(T)$ data suggest spin-glass ordering at about 50 K in both compounds arising from frustration and/or competing interactions, consistent with previous reports.^{21,26,27} From classical Monte Carlo simulations, Enjalran and coworkers concluded that single ion anisotropies are needed to explain the observed magnetic structures in this class of compounds, particularly the orthogonal ordering of the spins in adjacent layers observed²⁰ in $\text{Sr}_2\text{Mn}_3\text{Sb}_2\text{O}_2$.⁴³

On the other hand we find that $\text{Sr}_2\text{Mn}_2\text{CuAs}_2\text{O}_2$ exhibits a long-range ferrimagnetic transition as deduced from both magnetic susceptibility and neutron diffraction measurements. The latter measurements show a change in the magnetic ground state structure from a

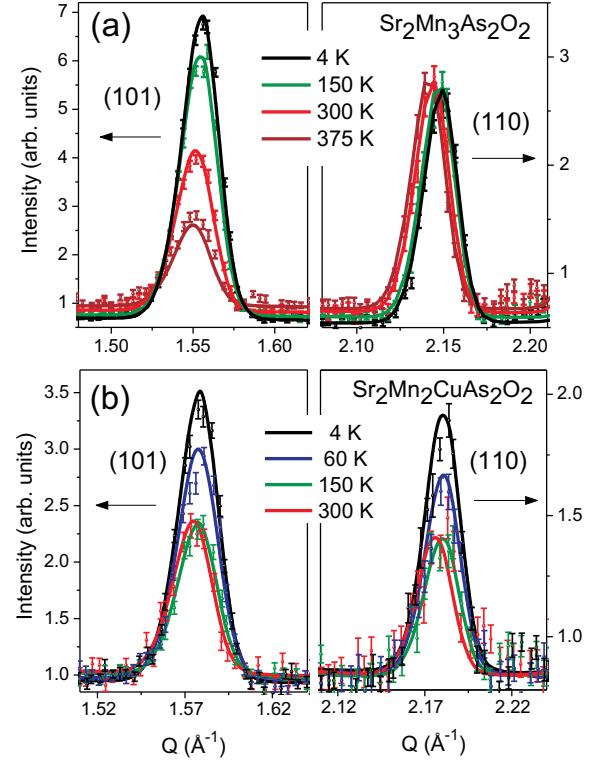


FIG. 15: (Color online) Temperature dependence of the intensity of the (101) and (110) diffraction peaks for (a) $\text{Sr}_2\text{Mn}_3\text{As}_2\text{O}_2$ and (b) $\text{Sr}_2\text{Mn}_2\text{CuAs}_2\text{O}_2$

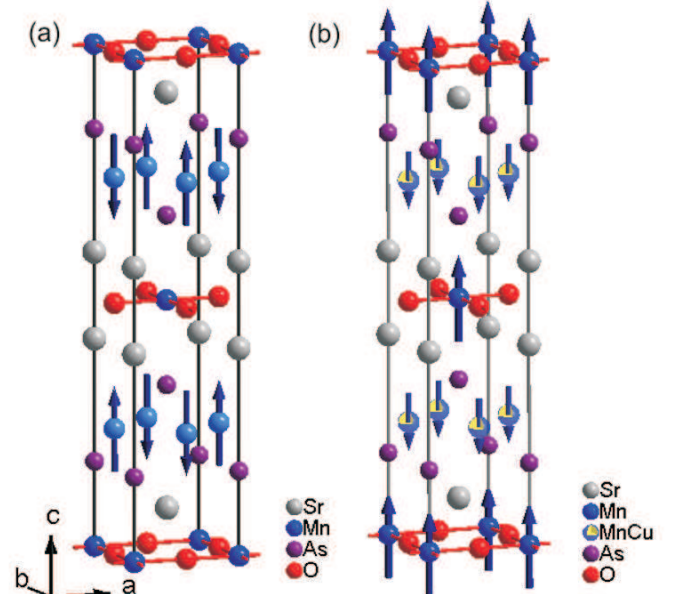


FIG. 16: (Color online) (a) Magnetic structure model used in the refinement of $\text{Sr}_2\text{Mn}_3\text{As}_2\text{O}_2$, consisting of antiferromagnetic ordering of the Mn2 site and (b) Ferrimagnetic structural model proposed for $\text{Sr}_2\text{Mn}_2\text{CuAs}_2\text{O}_2$, consisting of antiparallel alignment of Mn1 and Mn2 moments.

G-type antiferromagnetic structure in $\text{Sr}_2\text{Mn}_3\text{As}_2\text{O}_2$, in which only the Mn1 spins in the Mn_2As_2 layers appear to undergo three-dimensional long-range ordering [although the (100) magnetic peak we observe remains unexplained], to an A-type ferrimagnetic structure in $\text{Sr}_2\text{Mn}_2\text{CuAs}_2\text{O}_2$ in which the Mn1 ions in the MnO_2 layers now also exhibit long-range magnetic ordering. A steep increase of $\chi(T)$ and a bifurcation of the ZFC and FC $\chi(T)$ data in Fig. 8(a) suggest that the Curie temperature is $T_C \sim 80\text{--}100$ K. A more accurate determination of T_C was carried out using Arrott plots which gave $T_C = 95(1)$ K with mean-field critical exponents for the susceptibility and spontaneous magnetization. It is surprising and unexplained why our specific heat data for this compound show no discernable anomaly at T_C .

Our $\rho(T)$ data indicate that $\text{Sr}_2\text{Zn}_2\text{MnAs}_2\text{O}_2$ and $\text{Sr}_2\text{Mn}_3\text{As}_2\text{O}_2$ are both narrow band gap semiconductors with activation energies $\Delta = 147(5)$ meV and $133(4)$ meV, respectively. The Ba analogue $\text{Ba}_2\text{Zn}_2\text{MnAs}_2\text{O}_2$ is also reported to be a semiconductor with $\Delta \simeq 92.2$ meV (1070 K).⁴⁵

Partial substitution of Mn by Cu in $\text{Sr}_2\text{Mn}_3\text{As}_2\text{O}_2$ to form the new compound $\text{Sr}_2\text{Mn}_2\text{CuAs}_2\text{O}_2$ leads to a drastic change in $\rho(T)$ from any of the other compounds studied and we infer the ground state of this compound is probably metallic, consistent with our low temperature specific heat data that show a sizable linear specific heat coefficient. Single crystal resistivity measurements would be helpful to confirm this hypothesis. From our neutron diffraction studies, the Cu is found to statistically occupy 37(1)% of the metal sites in the FeAs-type layer together with 63(1)% of Mn. For comparison, BaMn_2As_2 , in which the FeAs-type layer is completely occupied by Mn, has an insulating ground state.^{34,46} On the other hand BaCu_2As_2 , in which the FeAs-type layer is completely occupied by Cu, is metallic.⁴⁸ Thus the inferred metallic ground state of $\text{Sr}_2\text{Mn}_2\text{CuAs}_2\text{O}_2$ is evidently specifically due to the presence of Cu in the FeAs-type layer.

The compounds $\text{Sr}_2\text{Zn}_2\text{MnAs}_2\text{O}_2$ and $\text{Sr}_2\text{Mn}_3\text{As}_2\text{O}_2$ also show large linear heat capacity coefficients at low temperatures that cannot arise from conduction carriers since these compounds are insulators at such temperatures. The values are similar to the value of 38.7 mJ/mol K² reported before for the Ba analogue $\text{Ba}_2\text{Zn}_2\text{MnAs}_2\text{O}_2$.⁴⁵ It is interesting in this context that the pure Ba compound $\text{Ba}_2\text{Mn}_3\text{As}_2\text{O}_2$ has a zero linear specific heat coefficient⁴⁵ as compared with the large value found for $\text{Sr}_2\text{Mn}_3\text{As}_2\text{O}_2$. Furthermore a significant difference was observed between the magnetic properties of these two compounds. The $\chi(T)$ of $\text{Ba}_2\text{Mn}_3\text{As}_2\text{O}_2$ shows a low-dimensional ordering at ~ 100 K with no bifurcation between the FC and ZFC data which would have indicated the occurrence of a spin-glass transition²¹ while we and others²¹ observed such a bifurcation at ~ 50 K suggesting a spin-glass or some other type of transition in $\text{Sr}_2\text{Mn}_3\text{As}_2\text{O}_2$. Therefore it seems that the occurrence of large linear specific heat coefficients and

the occurrence of spin-glass or possibly other types of transitions are closely related in this class of materials.

A comparison of the structural and magnetic properties the four compounds (1) $\text{Sr}_2\text{Mn}_3\text{Sb}_2\text{O}_2$, (2) $\text{Ba}_2\text{Zn}_2\text{MnAs}_2\text{O}_2$, (3) $\text{Sr}_2\text{Mn}_3\text{As}_2\text{O}_2$, and (4) $\text{Sr}_2\text{Zn}_2\text{MnAs}_2\text{O}_2$ has been given in Ref. 26. The c -axis lattice constant decreases in the listed order, and the magnetic properties of the MnO_2 sublattice show a systematic variation. For compounds (1) and (3), the MnAs sublattice orders above 300 K in a G-type antiferromagnetic structure, independent of the Mn in the MnO_2 sublattice. Apparently only for compound (1), the Mn in the MnO_2 planes orders at 65 K. Compounds (2) and (3) show two-dimensional short-range ordering and compound (4) with positive Weiss temperature θ shows no clear indication of any ordering. These systematic differences are attributed to the increasing level of ferromagnetic correlations as the c -axis and interlayer separation decrease. In $\text{Sr}_2\text{Mn}_2\text{CuAs}_2\text{O}_2$ the c lattice constant is smaller than in any of the above four mentioned compounds. Thus the A-type ferrimagnetic behavior of this compound is consistent with these trends.

V. SUMMARY

We have synthesized the layered compounds $\text{Sr}_2\text{Mn}_2\text{CuAs}_2\text{O}_2$, $\text{Sr}_2\text{Mn}_3\text{As}_2\text{O}_2$, and $\text{Sr}_2\text{Zn}_2\text{MnAs}_2\text{O}_2$ and investigated their physical properties systematically by means of x-ray and neutron diffraction, magnetic susceptibility, electrical resistivity, and heat capacity measurements. $\text{Sr}_2\text{Mn}_3\text{As}_2\text{O}_2$ and $\text{Sr}_2\text{Zn}_2\text{MnAs}_2\text{O}_2$ were found to be narrow band gap semiconductors with activation energies $\Delta = 133(4)$ and $147(5)$ K, respectively, while the new compound $\text{Sr}_2\text{Mn}_2\text{CuAs}_2\text{O}_2$ appears to have a metallic ground state. The metallic character is evidently due to the presence of Cu in the FeAs-type layer, and is also evidenced by a sizable linear specific heat coefficient.

Our magnetization, magnetic susceptibility, and neutron diffraction measurements indicated that $\text{Sr}_2\text{Mn}_2\text{CuAs}_2\text{O}_2$ is a ferrimagnet with a Curie temperature $T_C = 95(1)$ K whereas $\text{Sr}_2\text{Mn}_3\text{As}_2\text{O}_2$ and $\text{Sr}_2\text{Zn}_2\text{MnAs}_2\text{O}_2$ are evidently low-dimensional systems exhibiting spin-glass transitions at about 50 K due to competing ferromagnetic and antiferromagnetic interactions, although we do not rule out long-range order of the Mn1 spins in $\text{Sr}_2\text{Mn}_3\text{As}_2\text{O}_2$. Remarkably, we find that the magnetic ground state structure changes from a G-type antiferromagnetic structure in $\text{Sr}_2\text{Mn}_3\text{As}_2\text{O}_2$, in which only the Mn1 spins in the Mn_2As_2 layers order long-range and nearest-neighbor spins are antiparallel, to an A-type ferrimagnetic structure in $\text{Sr}_2\text{Mn}_2\text{CuAs}_2\text{O}_2$ in which the Mn ions in each layer are ferromagnetically aligned, but are antiferromagnetically aligned between layers.

It would be very interesting if a compound could be synthesized in which the Mn1 atoms in the MnO_2 lay-

ers of $\text{Sr}_2\text{Mn}_3\text{As}_2\text{O}_2$ were replaced by Cu and the Mn atoms in the MnAs layers replaced by Fe. This would give a compound with alternating CuO_2 and Fe_2As_2 layers which are the superconducting layer elements of the cuprate and pnictide high T_c superconductors, respectively. Although our efforts to accomplish this goal have not been successful so far as described above, this is still a promising direction for future synthesis efforts.

Acknowledgments

Work at the Ames Laboratory was supported by the Department of Energy-Basic Energy Science under Con-

tract No. DE-AC02-07CH11358. The work at the High Flux Isotope Reactor, Oak Ridge National Laboratory (ORNL), was sponsored by the Scientific User Facilities Division, Office of Basic Energy Sciences, U.S. Department of Energy (U.S. DOE). ORNL is operated by UT-Battelle, LLC for the U.S. DOE under Contract No. DE-AC05-00OR22725.

-
- * Present address: Indian Institute of Science Education and Research, Thiruvananthapuram-695016, Kerala, India
- ¹ J. G. Bednorz and K. A. Müller, *Z. Phys. B* **64**, 189 (1986).
 - ² A. Schilling, M. Cantoni, J. D. Guo, and H. R. Ott, *Nature* **363**, 56 (1993).
 - ³ L. Gao, Y. Y. Xue, F. Chen, Q. Xiong, R. L. Meng, D. Ramirez, C. W. Chu, J. H. Eggert, and H. K. Mao, *Phys. Rev. B* **50**, 4260 (1994).
 - ⁴ Z.-A. Ren, L. Wei, Y. Jie, Y. Wei, S. X. Li, Z. Cai, C. G. Can, D. X. Li, S. L. Ling, Z. Fang, and Z. Z. Xian, *Chin. Phys. Lett.* **25**, 2215 (2008).
 - ⁵ Y. Kamihara, T. Watanabe, M. Hirano, and H. Hosono, *J. Am. Chem. Soc.* **130**, 3296 (2008).
 - ⁶ X. H. Chen, T. Wu, G. Wu, R. H. Liu, H. Chen, and D. F. Fang, *Nature* **453**, 761 (2008).
 - ⁷ Z.-A. Ren, J. Yang, W. Lu, W. Yi, X.-L. Shen, Z.-C. Li, G.-C. Che, X.-L. Dong, L.-L. Sun, F. Zhou, and Z.-X. Zhao, *Europhys. Lett.* **82**, 57002 (2008).
 - ⁸ Y. Kamihara, H. Hiramatsu, M. Hirano, R. Kawamura, H. Yanagi, T. Kamiya, and H. Hosono, *J. Am. Chem. Soc.* **128**, 10012 (2006).
 - ⁹ M. Rotter, M. Tegel, and D. Johrendt, *Phys. Rev. Lett.* **101**, 107006 (2008).
 - ¹⁰ G. F. Chen, Z. Li, G. Li, W.-Z. Hu, J. Dong, J. Zhou, X.-D. Zhang, P. Zheng, N.-L. Wang, and J.-L. Luo, *Chin. Phys. Lett.* **25**, 3403 (2008).
 - ¹¹ H. S. Jeevan, Z. Hossain, D. Kasinathan, H. Rosner, C. Geibel, and P. Gegenwart, *Phys. Rev. B* **78**, 092406 (2008).
 - ¹² K. Sasmal, B. Lv, B. Lorenz, A. M. Guloy, F. Chen, Y.-Y. Xue, and C. W. Chu, *Phys. Rev. Lett.* **101**, 107007 (2008).
 - ¹³ G. Wu, H. Chen, Y. L. Xie, Y. J. Yan, R. H. Liu, X. F. Wang, J. J. Ying, and X. H. Chen, *J. Phys.: Condens. Matter* **20**, 422201 (2008).
 - ¹⁴ J. P. Attfield, A. L. Kharlanov, and J. A. McAllister, *Nature* **394**, 157 (1998).
 - ¹⁵ J. G. Lin, C. Y. Huang, Y. Y. Xue, C. W. Chu, X. W. Cao, and J. C. Ho, *Phys. Rev. B* **51**, 12900 (1995).
 - ¹⁶ M. Varela, D. Arias, Z. Sefrioui, C. Leon, C. Ballesteros, S. J. Pennycook, and J. Santamaria, *Phys. Rev. B* **66**, 134517 (2002).
 - ¹⁷ L. M. Volkova, *Supercond. Sci. Technol.* **21**, 095019 (2008).
 - ¹⁸ T. C. Ozawa and S. M. Kauzlarich, *Sci. Technol. Adv. Mater.* **9**, 033003 (2008).
 - ¹⁹ E. Brechtel, G. Cordier, and H. Schäfer, *Z. Naturforsch.* **34b**, 777 (1979).
 - ²⁰ S. L. Brock, N. P. Raju, J. E. Greedan, and S. M. Kauzlarich, *J. Alloys Comp.* **237**, 9 (1996).
 - ²¹ S. L. Brock and S. M. Kauzlarich, *J. Alloys Comp.* **241**, 82 (1996).
 - ²² N. T. Stetson and S. M. Kauzlarich, *Inorg. Chem.* **30**, 3969 (1991).
 - ²³ Y. Park, D. C. DeGroot, J. L. Schindler, C. R. Kannewurf, and M. G. Kanatzidis, *Chem. Mater.* **5**, 8 (1993).
 - ²⁴ W. J. Zhu, P. H. Hor, A. J. Jacobson, G. Crisci, T. A. Albright, S.-H. Wang, and T. Vogt, *J. Am. Chem. Soc.* **119**, 12398 (1997); W. J. Zhu and P. H. Hor, *J. Solid State Chem.* **134**, 128 (1997); W. J. Zhu and P. H. Hor, *J. Solid State Chem.* **130**, 319 (1997).
 - ²⁵ D. Kaczorowski, J. H. Albering, H. Noël, and W. Jeitschko, *J. Alloys Compd.* **216**, 117 (1994); R. Pöttgen, B. Chevalier, P. Gravereau, B. Darriet, W. Jeitschko, and J. Etourneau, *J. Solid State Chem.* **115**, 247 (1995).
 - ²⁶ T. C. Ozawa, S. M. Kauzlarich, M. Bieringer, C. R. Wiebe, J. E. Greedan, and J. S. Gardner, *Chem. Mater.* **13**, 973 (2001).
 - ²⁷ T. Ozawa, M. M. Olmstead, S. L. Brock, S. M. Kauzlarich, and D. M. Young, *Chem. Mater.* **10**, 392 (1998).
 - ²⁸ S. L. Brock and S. M. Kauzlarich, *ChemTech.* **25**, 18 (July, 1995).
 - ²⁹ V. O. Garlea, B. C. Chakoumakos, S. A. Moore, G. B. Taylor, T. Chae, R. G. Maples, R. A. Riedel, G. W. Lynn, and D. L. Selby, *Appl. Phys. A* (in press) DOI 10.1007/s00339-010-5603-6.
 - ³⁰ J. Rodriguez-Carvajal, *Physica B* **192**, 55 (1993). The Rietveld refinement program is available at <<http://www.ill.eu/sites/fullprof/>>.
 - ³¹ B. Morosin, *Phys. Rev. B* **1**, 236 (1970).
 - ³² A. C. Larson and R. B. Von Dreele, "General Structure Analysis System (GSAS)", Los Alamos National Laboratory Report LAUR 86-748 (2000); B. H. Toby, *J. Appl. Cryst.* **34**, 210 (2001).
 - ³³ P. W. Selwood, *Magnetochemistry*, 2nd ed. (Interscience, New York, 1956), p. 78.
 - ³⁴ J. An, A. S. Sefat, D. J. Singh, and M.-H. Du, *Phys. Rev. B* **79**, 075120 (2009).
 - ³⁵ C. P. Bean and D. S. Rodnell, *Phys. Rev.* **126**, 104 (1962).
 - ³⁶ S. Haneda, N. Kazama, Y. Yamaguchi, and H. Watanabe, *J. Phys. Soc. Jpn.* **42**, 1201 (1977).

- ³⁷ Z. He, Y. Ueda, and M. Itoh, *Solid State Commun.* **141**, 22 (2007).
- ³⁸ C. Kittel, *Introduction to Solid State Physics*, 4th ed. (Wiley, New York, 1966).
- ³⁹ A. Arrott, *Phys. Rev.* **108**, 1394 (1957).
- ⁴⁰ W. Knafo, C. Meingast, A. V. Boris, P. Popovich, N. N. Kovaleva, P. Yordanov, A. Maljuk, R. K. Kremer, H. v. Löhneysen, and B. Keimer, *Phys. Rev. B* **79**, 054431 (2009).
- ⁴¹ R. L. Hadimani, Y. Melikhov, J. E. Snyder, and D. C. Jiles, *J. Magn. Magn. Mater.* **320**, e696 (2008).
- ⁴² F. J. Castaño, J. M. García-Beneytez, P. Crespo, M. Multiñer, M. Vazquez, and A. Hernando, *J. Phys.: Condens. Matter* **11**, 5671 (1999).
- ⁴³ M. Enjalran, R. T. Scalettar, and S. M. Kauzlarich, *Phys. Rev. B* **61**, 14 570 (2000).
- ⁴⁴ <<http://www.ncnr.nist.gov/resources/n-lengths/list.html>>.
- ⁴⁵ A. Matsushita, T. C. Ozawa, J. Tang, and S. M. Kauzlarich, *Physica B* **284-288**, 1424 (2000).
- ⁴⁶ Y. Singh, A. Ellern, and D. C. Johnston, *Phys. Rev. B* **79**, 094519 (2009).
- ⁴⁷ R. Nath, Y. Singh, and D. C. Johnston, *Phys. Rev. B* **79**, 174513 (2009).
- ⁴⁸ D. J. Singh, *Phys. Rev. B* **79**, 153102 (2009).